The Thesis Committee for Cheng Tan
Certifies that this is the approved version of the following thesis:

WSe_2-Based Devices and Oxide Structures

APPROVED BY
SUPERVISING COMMITTEE:

Supervisors:

____
Deji Akinwande

____
Rodney S. Ruoff

WSe_2-Based Devices and Oxide Structures

By

Cheng Tan, B.S.

Thesis

Presented to the Faculty of the Graduate School of

The University of Texas at Austin

in Partial Fulfillment

of the Requirements

for the Degree of

Master of Science in Engineering

The University of Texas at Austin

May 2014

Acknowledgements

This work would not be possible without my advisors Professors Rodney S. Ruoff and Deji Akinwande. They have assisted me with invaluable advice and insight along the way. In addition, I would like to thank Yingnan Liu, Professor Keji Lai, Avinash Nayak, Professor Jung-fu Lin, Sherry Chang, Xiaohan Wang, Dr. Richard Piner, Dr. Karalee Jarvis, Dr. Jiping Zhou, and Harry Chou for their assistance and discussions. I am grateful for my funding sources: the Cockrell School of Engineering at the University of Texas at Austin and the National Defense Science and Engineering Graduate Fellowship program. They have assisted me immensely throughout the graduate process.

I thank my family and friends as well as everyone around me for their support and assistance.

Abstract

WSe_2-Based Devices and Oxide Structures

Cheng Tan, M.S.E.

The University of Texas at Austin, 2014

Supervisor: Deji Akinwande

Co-Supervisor: Rodney S. Ruoff

In this work the transition metal dichalcogenide WSe_2 is exfoliated and characterized. It is shown from the electrical measurements that the material can display both p-type conduction as well as ambipolar characteristics. WSe_2 flakes were also oxidized through thermal and laser treatments to produce oxide structures. The structures and oxidation processes are characterized and described in this thesis.

Table of Contents

List of Figures

Chapter 1: Introduction

A brief introduction to two dimensional (2D) materials is given in this chapter. A rough overview of graphene and h-BN is presented in 1.1, and transition metal dichalcogenides will be discussed in 1.2.

1.1 Two Dimensional Materials

2D materials are structurally planar materials that display highly anisotropic properties, having different in-plane and out-of-plane characteristics. The materials, at atomically thin layers, are known to exhibit novel properties that differ from their bulk counterpart.

One such 2D material, which has been the primary material of research in this field for the past decade, is graphene. Since the successful isolation and characterization of graphene, an atomic layer of sp^2 bonded carbon, vast amounts of interest has been generated in researching the material's properties and devices. [1, 2]. Graphene and graphene-derived materials have been considered for a wide array of applications including flexible electronics [3, 4], energy storage [5], plasmonics [6], high frequency electronics [7], and more. The interest in graphene sparked widespread investigations in other 2D materials, which includes hexagonal boron nitride (h-BN), transition metal dichalcogenides (TMDCs), phosphorene, and transition metal oxides among others. **Figure 1.1** shows a few of the 2D material structures.

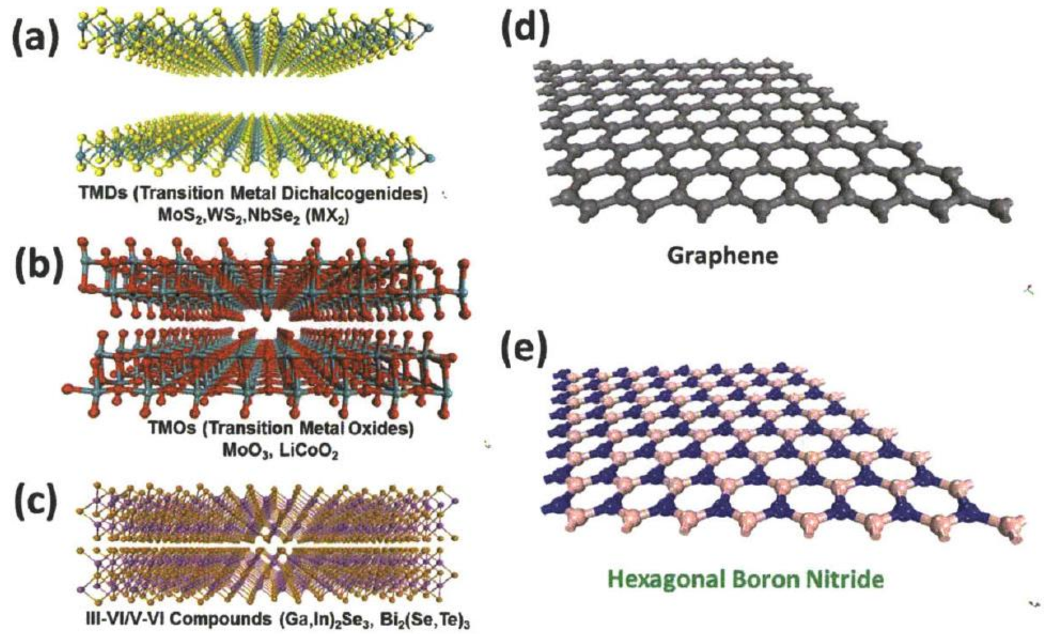

Figure 1.1. Structure of 2D materials. The structures of (a) transition metal dichalcogenides, (b) transition metal oxides, (c) III-VI/V-VI compounds, (d) graphene, and (e) hexagonal boron nitride are shown. [8]

Among these materials, h-BN has been studied as a dielectric for graphene due to its wide band gap, structural similarity (1.8% lattice mismatch), chemically inert stability and atomic flatness [9, 10]. On h-BN, graphene can achieve much higher mobility values than that on top other dielectrics such as SiO_2 [9]. These properties has led to the research of encapsulating other 2D materials such as graphene within h-BN to reduce the extrinsic environmental effects that may occur during or after processing [11]. Beyond graphene, TMDCs are currently under investigation for their intrinsic band gaps, which offer higher current on/off ratios for electronic applications. The transition to a direct energy band gap in various TMDCs at the monolayer limit also opens up possibilities optoelectronic applications. [12]

The stacking of these 2D materials to create vertical heterostructures has become an increasingly pursued area of recent research [13]. By selectively layering 2D materials in varying configurations, it's possible to achieve numerous structures for different analyses and applications. **Figure 1.2** shows one such structure, an alternately layered bilayer graphene and h-BN superlattice, as imaged by scanning transmission electron microscopy (STEM) [14]. These heterostructures introduce additional directions in the research of two dimensional materials.

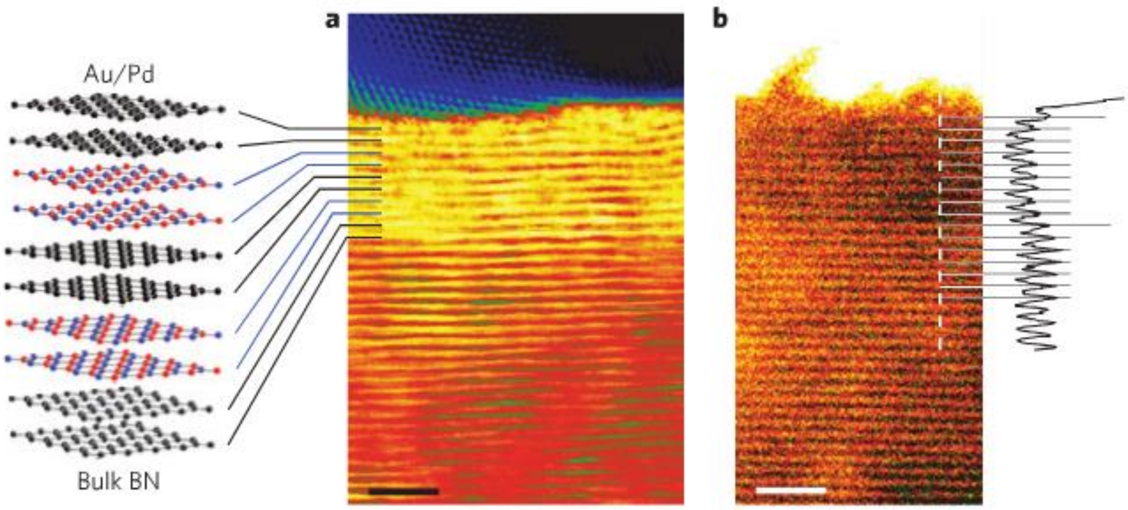

Figure 1.2 (a) Schematic and bright field STEM of a graphene bilayer and h-BN stacked superlattice. The high-angle annular dark field (HAADF) STEM is shown in (b) along with the intensity line profile of the layers. [14]

1.2 Transition Metal Dichalcogenides

TMDCs are of the chemical composition MX_2, where M is the metal and X is the chalcogenide, e.g. S, Se, etc. These materials are layered in the structure, where each TMDC layer contains three atomic layers: one layer of transition metal bonded to two chalcogenide layers, one below and one above. In materials with more than one TMDC layer, the layers are held together by weak van der Waals interactions between the layers. The layers can be stacked in 3 different ways, shown in **Figure 1.3**. [12]

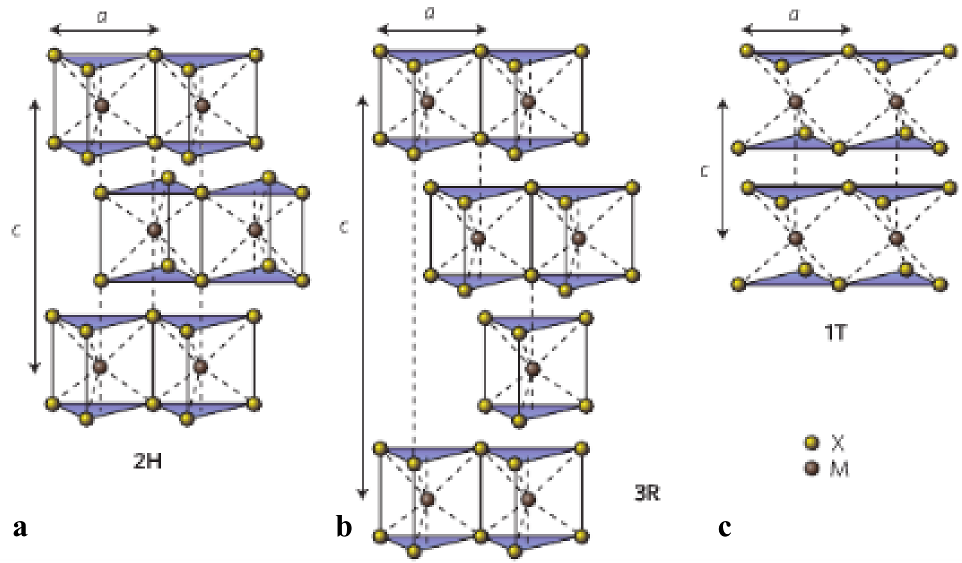

a **b** **c**

Figure 1.3. The possible stacking configurations of MX_2. (a) The 2H hexagonal configuration repeats every two layers. (b) The 3R rhombohedral configuration repeats every 3 layers. (c)The 1T tetragonal configuration repeats every layer. [12]

At atomically thin layers, the band structure in semiconducting TMDCs changes from that of bulk, as depicted in **Figure 1.4** for MoS_2 and WS_2.[12] The direct band gap at the K point remains much unchanged, but near the Γ point the indirect band gap is increased, and the direct band gap at K becomes the lowest energy gap.[15]

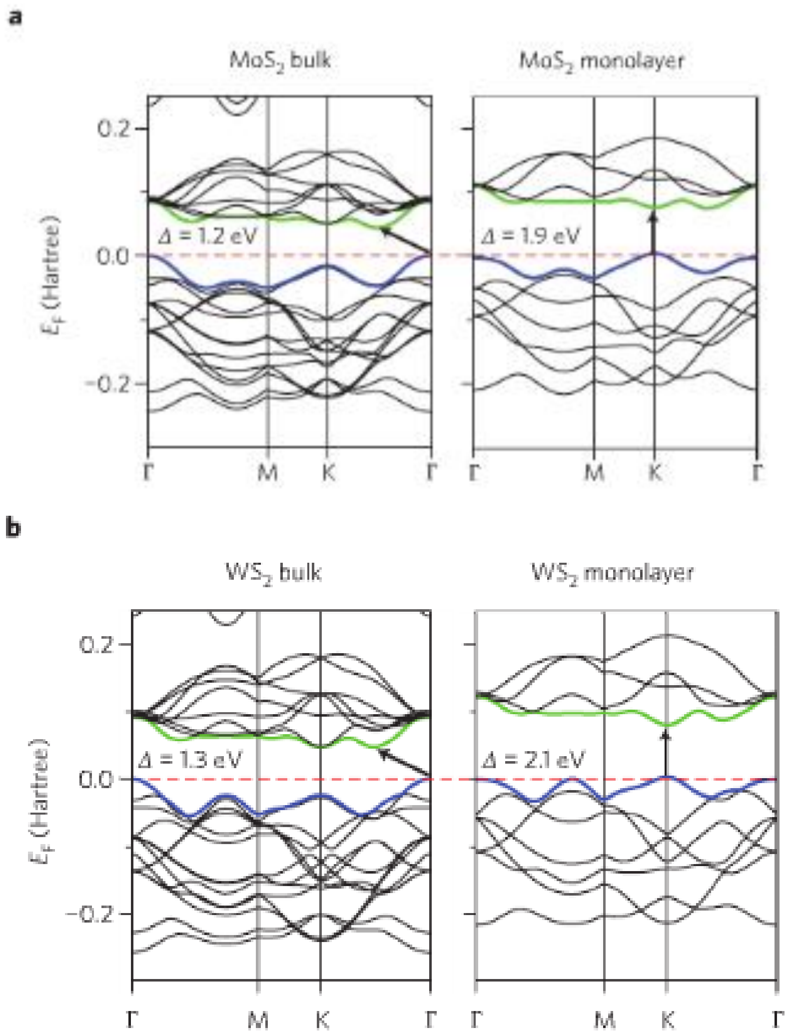

Figure 1.4. Band diagrams for MoS_2 bulk (a, left), MoS_2 monolayer (a, right), WS_2 bulk (b, left), and WS_2 monolayer (b, right). As the semiconducting TMDCs transitions from bulk to monolayer, the band structure transitions into a larger direct band gap from an indirect band gap. [15]

The existence of a band gap in TMDCs has led to much interest in their electronic applications as two dimensional materials. Research in this area include electronic characterization[16] and contact materials[17], logic devices[18], flexible electronics[19], as well as optoelectronics[20]. In addition, the TMDCs has been researched in vertical heterostructures in an effort to combine the electronic band gap with the high mobility of graphene, shown in **Figure 1.5** [21]. By using WS_2 as an intermediate layer between graphene layers, a ~10^6 on/off ratio is achieved via the TMDC band gap, which serves a tunnel barrier for carrier injection.

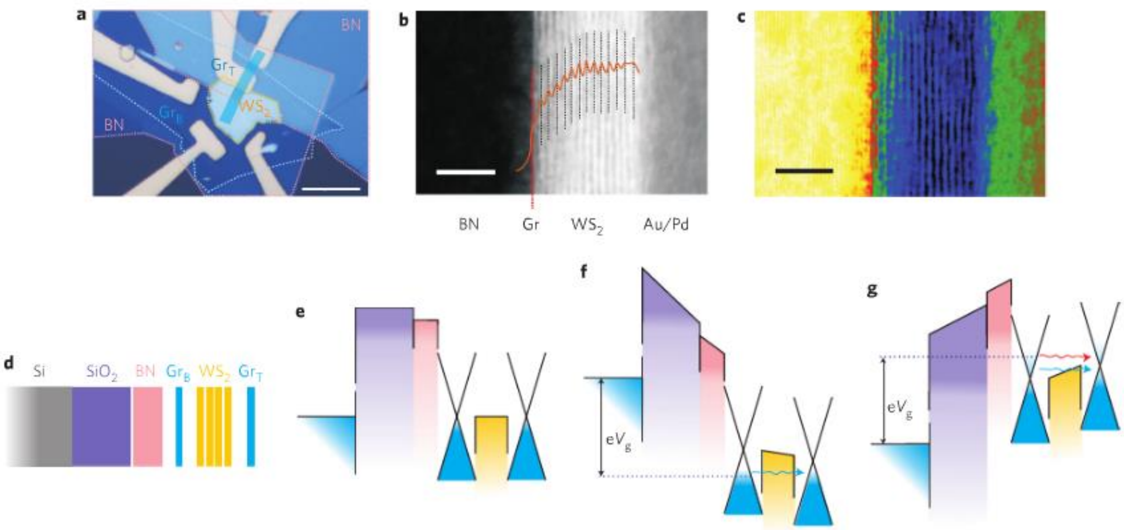

Figure 1.5. (a) Optical image (scale bar, 10 mm). (b) Cross-section high-resolution high-angle annular dark-field scanning transmission electron microscopy (HAADF STEM) image (scale bar, 5 nm). (c) Bright-field STEM image (scale bar, 5 nm). (d) Schematic of vertical architecture of transistor. (e) Band diagram corresponding to no V_g and applied V_b. (f) Negative V_g shifts the Fermi level of the two graphene layers down from the neutrality point, increasing the potential barrier and switching the transistor OFF. (g) Applying positive V_g results in an increased current between Gr_B and Gr_T (bottom and top graphene layers, respectively) due to both thermionic (red arrow) and tunneling (blue arrow) contributions. [21]

Among structures, molybdenum oxide (MoOx) has been researched as contact layer to MoS_2 field effect transistors, where the high work function of substoichiometric MoOx is used for hole injection into the MoS_2 layer [22]. In this work, the primary focus will be on the specific TMDC WSe_2 and its properties as well as the processes of obtaining lateral WSe_2-oxide structures. These processes and the obtained structures are characterized in order to shed light on the resulting materials.

Chapter 2: Preparation of WSe_2

This chapter outlines the characterization of the WSe_2, as acquired and exfoliated from bulk.

2.1 Exfoliation of WSe_2

To characterize and fabricate structures as well as devices from WSe_2, the standard mechanical exfoliation technique was used to obtain flakes from a bulk crystal. WSe_2 purchased from NanoSurf and 2DSemiconductors were exfoliated using Scotch® Magic™ ('magic') and UltraTape® 1310TB100-P5D ('blue') tape. Transmission electron microscopy (TEM) images of the WSe_2 flake are shown in **Figures 2.1a-b**. The atomic structure, which is layered in the out of plane direction and hexagonal within the plane, is shown in the **Figure 2.1c**. (Images were taken with the assistance of Dr. Karalee Jarvis, Avinash Nayak, Maria Hall, and Dr. Jiping Zhou.) 90 nm and 270 nm SiO_2/Si were used as substrates during the exfoliation for enhanced optical contrast; as shown by simulated results in **Figure 2.2**:TMDCs are typically visible on 50-100 nm and 200-300 nm SiO_2 substrates [23]. Both tapes were observed to leave behind residues, the magic tape especially so, as shown in the atomic force microscopy (AFM) map in **Figure 2.3a**. The residue left behind by magic tape can be alleviated via a 400 ºC degree anneal in an Ar/H_2 (50/1) atmosphere for ~1 hr. (**Figure 2.3b)**. Residue from the blue tape, while observably fewer, is less readily broken down by the annealing process. The blue tape was also detected by AFM to sometimes leave behind smaller flakes during the exfoliation process (**Figure 2.4**). For the remainder of this work, unless otherwise noted, the flakes were exfoliated with magic tape and annealed in 50/1 Ar/H_2 atmosphere for ~1 hr. at 400 ºC prior to additional processing.

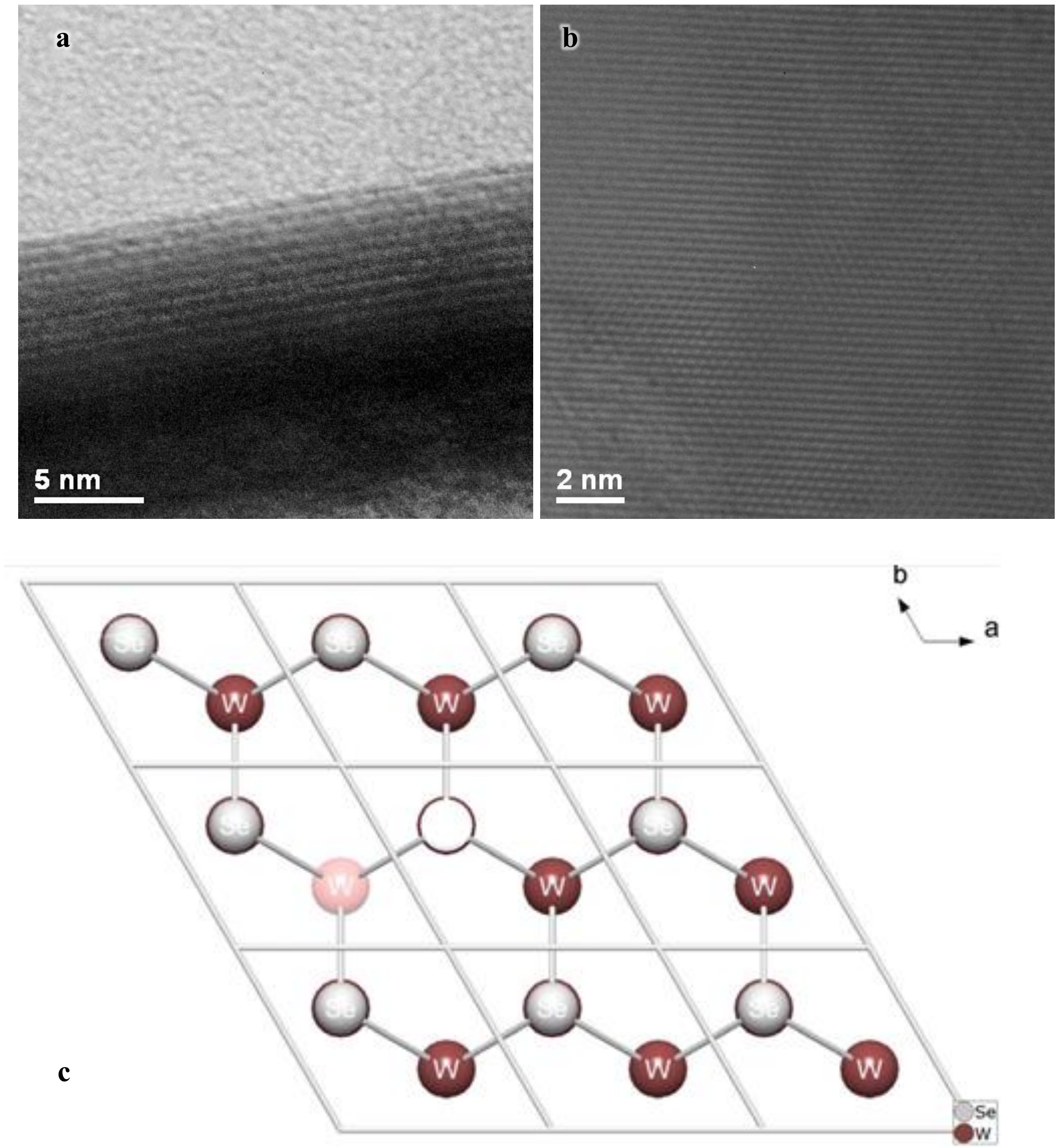

Figure 2.1. (a) Cross-sectional and (b) plain-view TEM image of WSe_2 flakes, clearly showing the layered structure and hexagonal lattice, as displayed in the schematic (c).

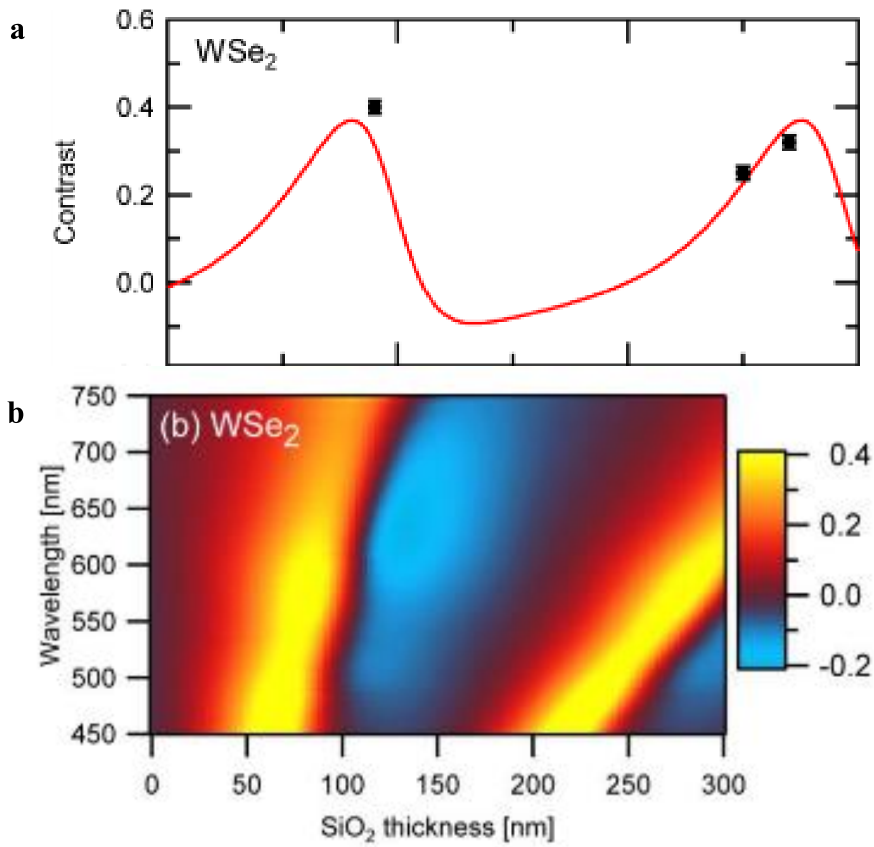

Figure 2.2. (a) Calculated (red) experimental (black) contrasts for broadband illumination detected with the green channel (495-530nm) of a camera. (b) A color plot of contrast as function of SiO_2 substrate thickness and incident wavelength. [23]

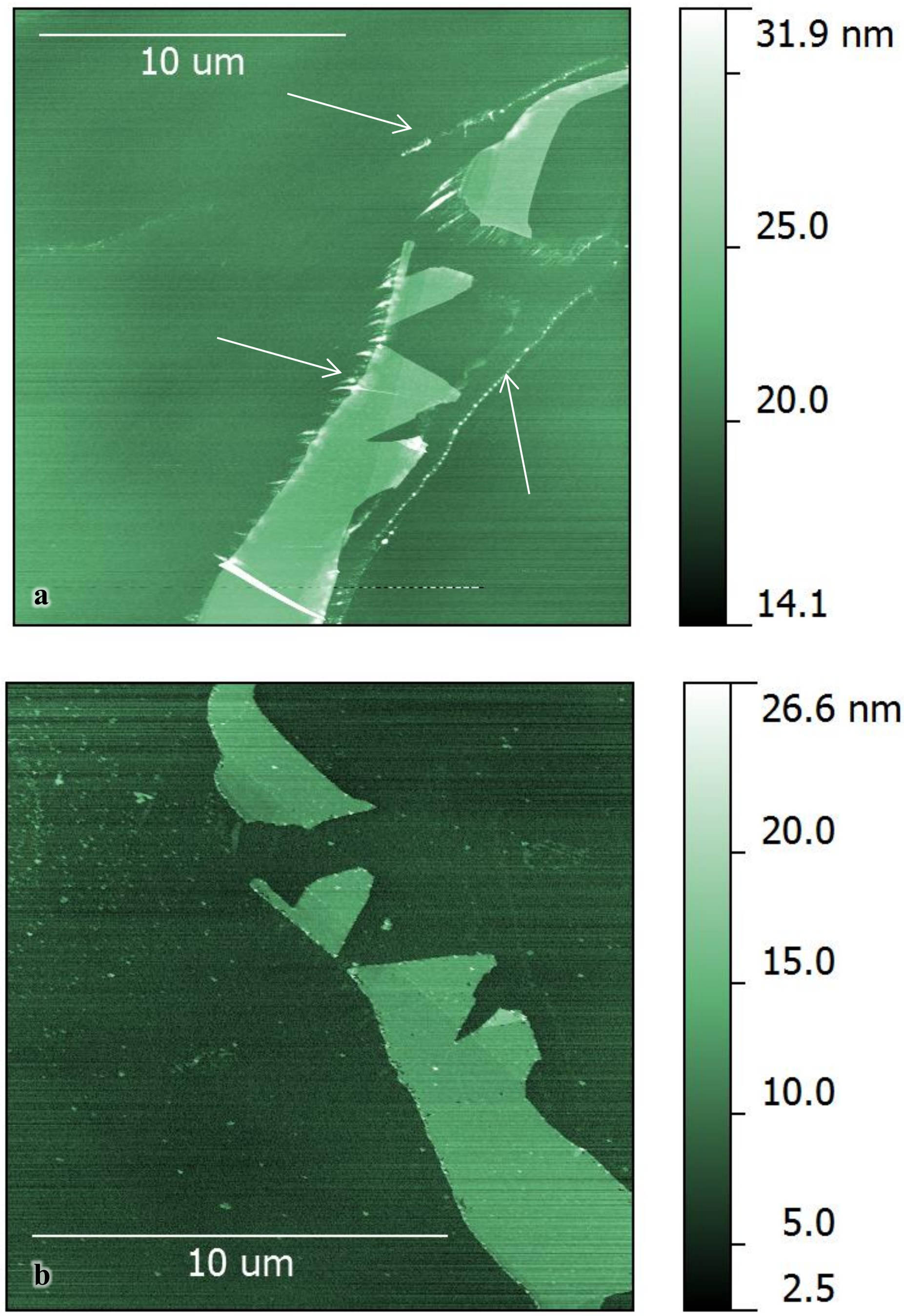

Figure 2.3. AFM images of a WSe_2 multilayer flake exfoliated with Scotch® Magic™ tape (a) before and (b) after hour-long anneal in Ar/H_2 at 400 °C. The continuous residue (marked by arrows) in (a) is observed to have broken down after the anneal (b).

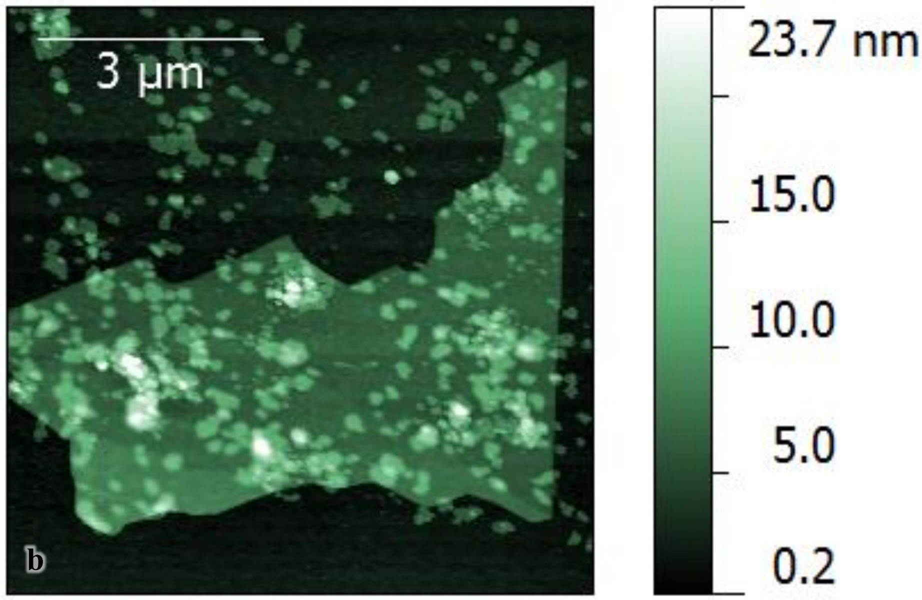

Figure 2.4. AFM image of a WSe_2 multilayer flake exfoliated with blue tape. Small mini flakes are scattered throughout the entire area.

2.2 Material Properties and Characterization

Figure 2.5 shows the band structure of WSe_2, like that of other semiconducting TMDCs (e.g. MoS_2, WS_2, etc.), shifts from a lower indirect band gap for the bulk crystal to a higher direct band gap as it becomes atomically thin [24]. At the K point, the direct excitonic transition is relatively unaffected by layer thickness whereas the indirect gap transition between the K and Γ points increases with decreasing thickness [24]. Such a phenomenon has been attributed to quantum confinement and resulting changes in the hybridization of orbitals in previous literature [12].

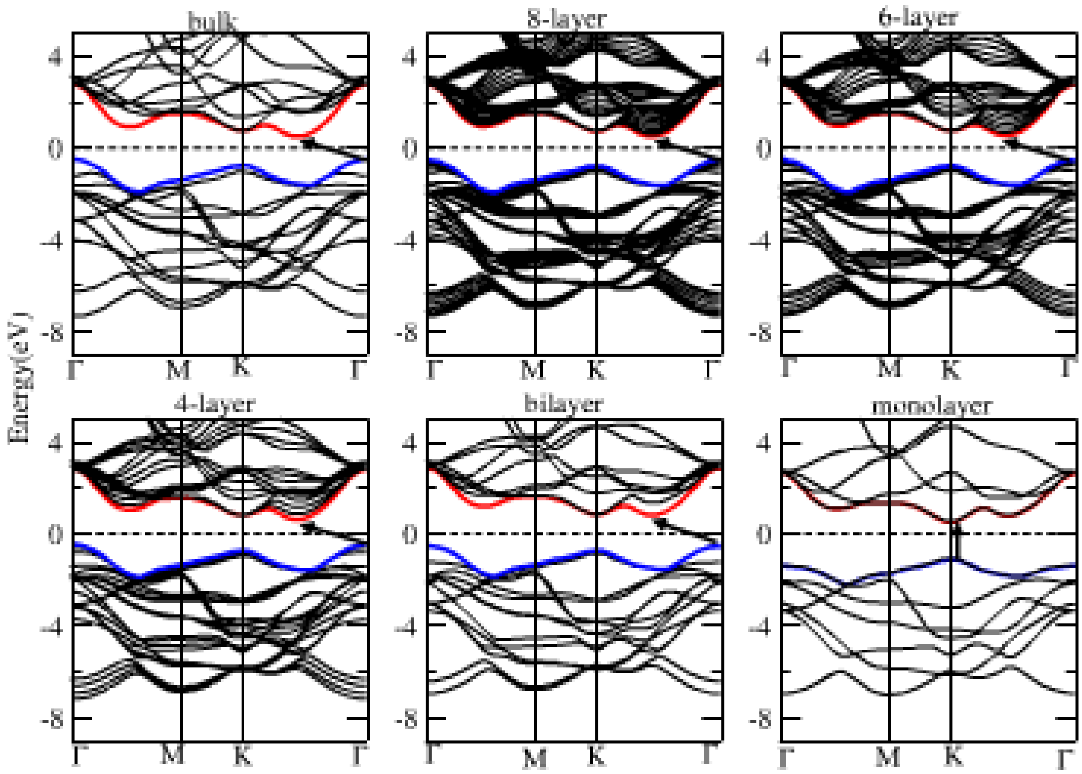

Figure 2.5. The calculated band structure for bulk-to-monolayer WSe_2, as labeled. The red outlines the lower most conduction band and blue outlines the uppermost valence band. At monolayer thickness, the lowermost valley of the conduction band occurs at the K point, forming the direct band gap. [24]

WSe_2 can be identified by its unique Raman signature, due to the active Raman modes shown in **Figure 2.6**. Of the four active Raman modes, E^1_{2g} and A_{1g} are observed experimentally [25]. However, the laser wavelength also plays a role in the optical signature. Twin Raman peaks at 248 cm^{-1} and 257 cm^{-1} (corresponding to E^1_{2g} and A_{1g}, respectively) are extracted using a 532 nm laser for ~5 layer WSe_2 sample exfoliated on 25 nm Al_2O_3/Si (**Figure 2.7)**. The peak at ~257 cm^{-1} is greatly diminished for the lower laser wavelength 442 nm comparatively. A peak was also observed at ~ 310 cm^{-1}, which has been attributed to different modes in literature. [26] The 532 nm laser also revealed additional peaks: the $2E_{1g}$ peak at ~355 cm^{-1}, the A_{1g}+LA at ~372 cm^{-1}, and the $2A_{1g}$-LA at ~395 cm^{-1}, where LA is the longitudinal acoustic phonon [27].

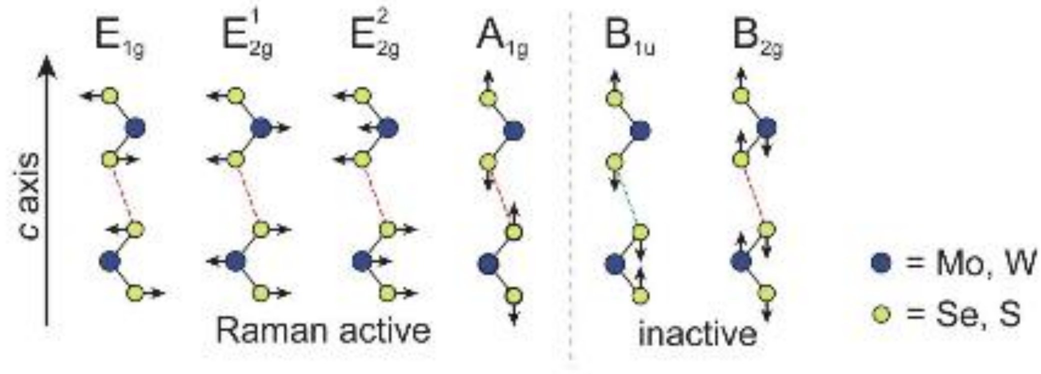

Figure 2.6. Schematic of Raman modes in TMDCs, the yellow represents the chalcogens and the blue is the transition metal. Of these modes, typically E^1_{2g} and A_{1g} are experimentally observed. [25]

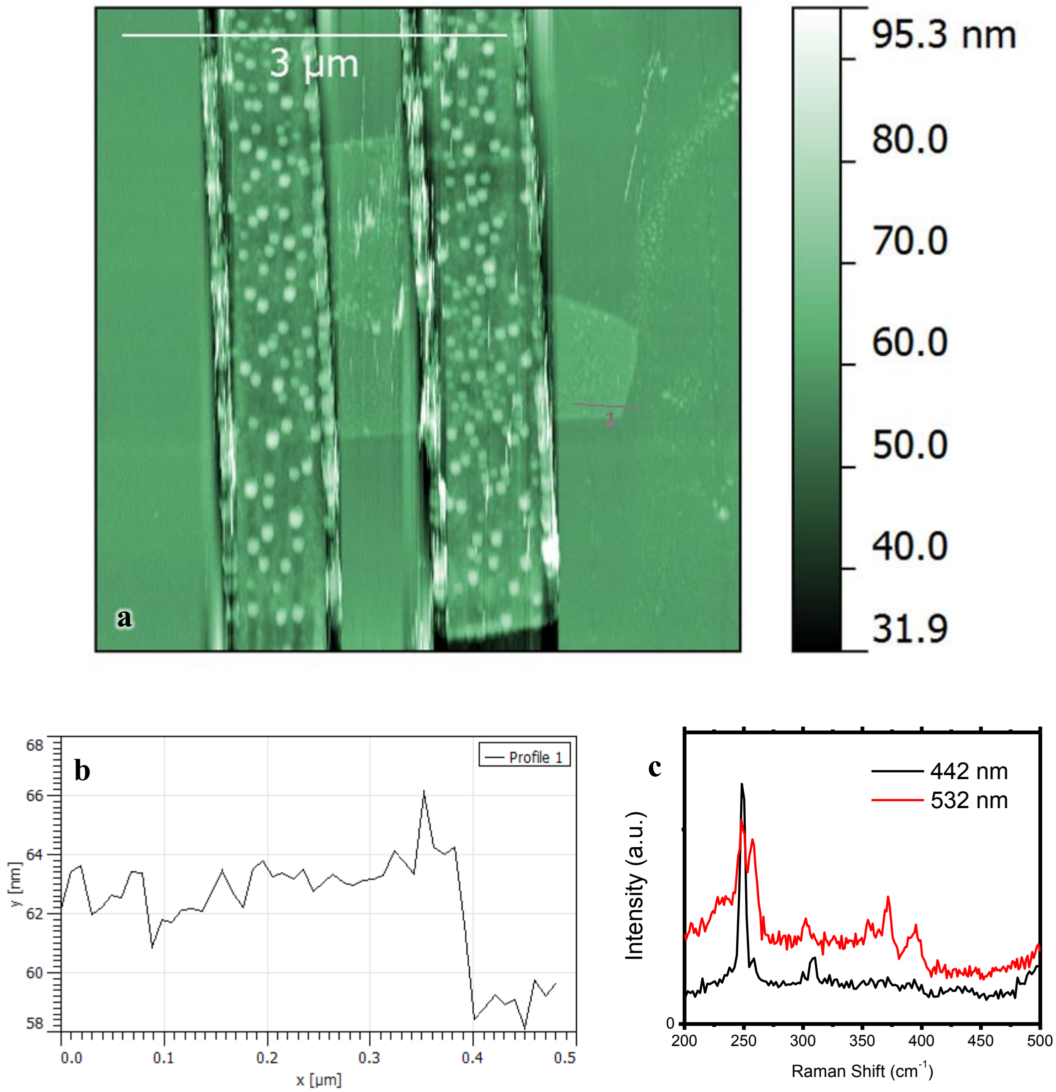

Figure 2.7. (a, top) AFM image of a few-layer WSe_2 flake after contact deposition. The line profile is shown in (b), with a step height of ~4 nm. (c) Raman spectroscopy measurements were taken of the flake using both a 442 nm laser and a 532 nm laser, exhibiting different signatures.

Microwave impedance microscopy (MIM) and simultaneous AFM measurements of exfoliated WSe_2 on 270 nm SiO_2/Si were completed through collaborations with Yingnan Liu of Professor Keji Lai's group, as shown in **Figure 2.8**. The imaginary and real maps show that the conductivity of the flakes changes with the layer thickness. From these plots, we can see qualitatively that thicker flakes have exhibit higher measured conductivity, whereas the conductivity of the monolayer region is close to that of the background SiO_2. It is noted that these are measured without a back gate voltage applied, and the semiconducting material is not considered to be "on."

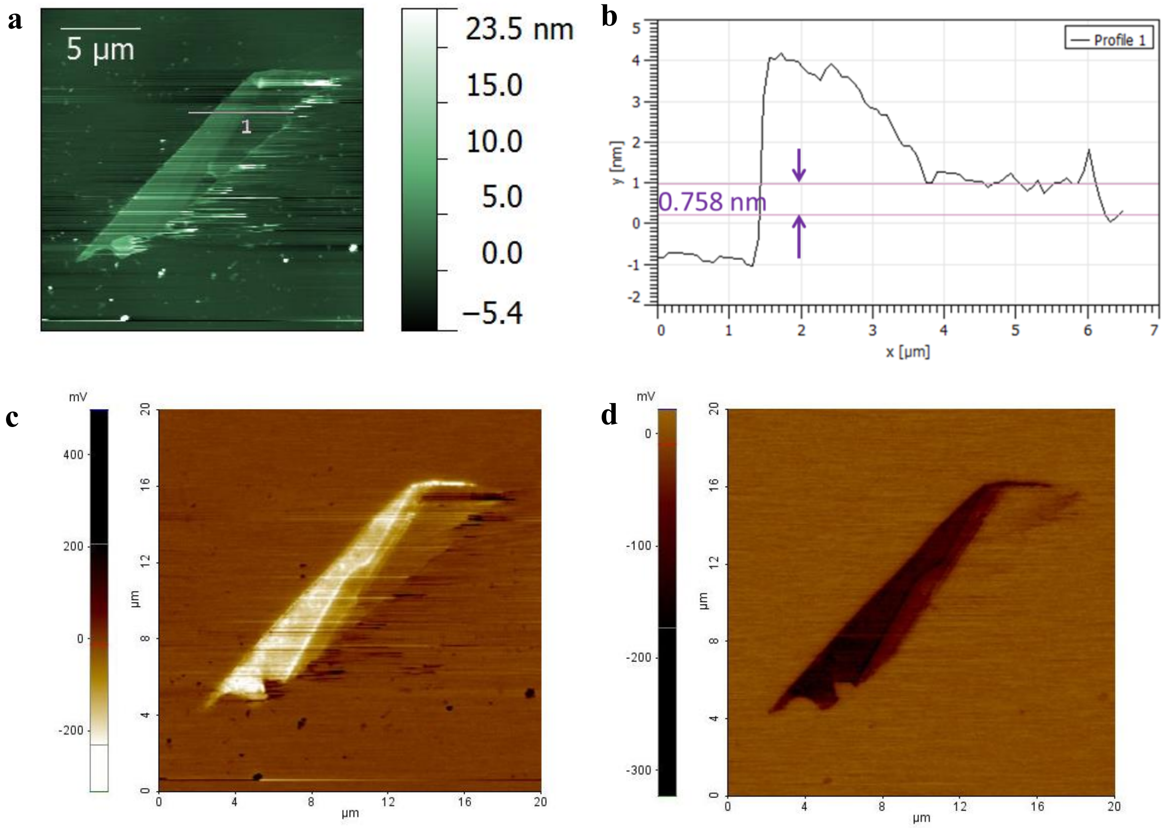

Figure 2.8. (a, top left) AFM image of an exfoliated flake; the monolayer region is outlined in the line profile, as shown in (b, top right). (c, bottom left) Imaginary and (d, bottom right) real parts of impedance maps, as obtained from microwave impedance microscopy.

Chapter 3: Fabrication and Characterization of WSe_2 Devices

In this chapter, the electronic characteristics of WSe_2 are presented. Section 3.1 outlines the fabrication methods of WSe_2 field effect transistors, and 3.2 outlines the measured electrical properties.

3.1 Device Fabrication

Back-gated field effect transistors were made from exfoliated WSe_2 flakes using electron beam lithography. The sample was coated with PMMA 495 A4 via spin coating at ~4000 rpm for ~40 s and baked with a hot plate at ~ 150 ºC for 2 min prior to electron-beam exposure and development. ~50 nm Pd contacts were then fabricated via electron beam evaporation and subsequent acetone liftoff. **Figure 2.7** shows the AFM image of a fabricated device, and **Figure 3.1** shows the optical image of a typical device.

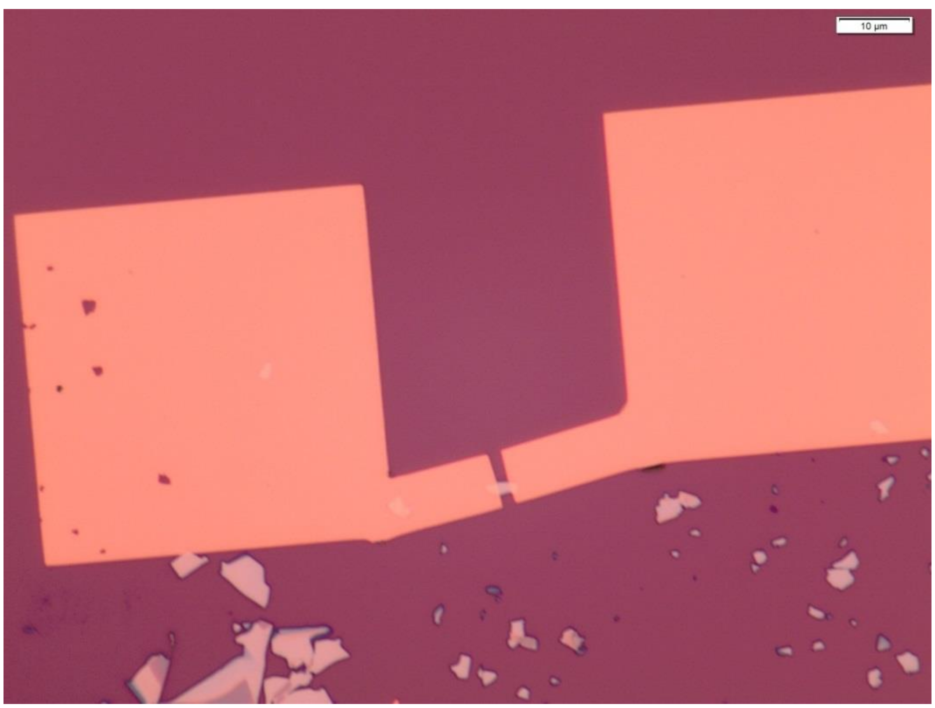

Figure 3.1. Optical image of a typical device fabricated using electron beam lithography after contact evaporation and lift off.

3.2 Device Characterization

Figure 3.2a shows the AFM map of a ~9 nm WSe_2 flake exfoliated onto 90 nm SiO_2/Si, which was then fabricated into a device with ~45 nm Pd contacts; the inset shows the profile across the flake. The drain-source current I_D was measured as a function of the back gate voltage V_G for the device at drain voltages V_D = -0.1 V and V_D = -1 V, in ambient atmosphere (**Figure 3.2b**). The '- to +' and '+ to -' denote the V_G sweep direction. The device shows clear p-type conduction with an on/off ratio of $\sim 10^6$ and a large hysteresis. This hysteresis is hypothesized to be caused by adsorbed molecules on the surface of the flake (e.g. water); the same device measured under 10^{-5} mbar vacuum atmosphere shows much less hysteresis, as shown in **Figure 3.2c**. In **Figure 3.2c**, the on/off ratio is $\sim 10^8$, two orders of magnitude higher than that measured under ambient atmosphere, despite a smaller V_G range (-40 V to 40 V as opposed to -60 V to 60 V). I_D-V_D characteristics (observed in **Figure 3.2d**) show the linear operation mode and the onset of saturation. Using the Y-function method, the device was extracted to have a low-field carrier mobility of ~50 $cm^2/V \cdot s$ and a contact resistance upper bound of ~60 $\Omega \cdot mm$ [28, 29].

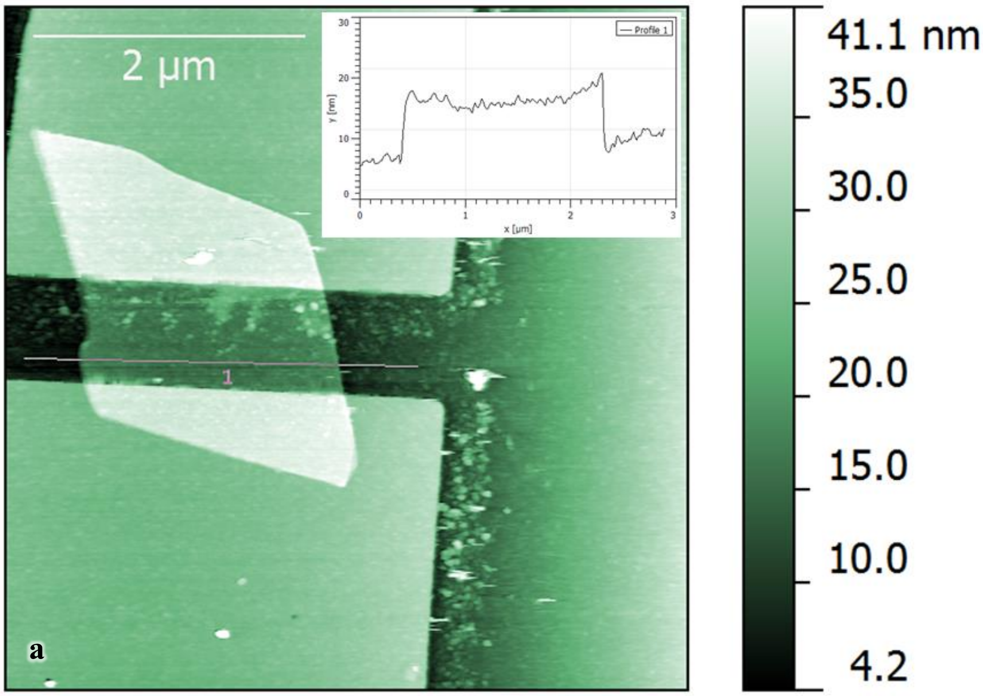

2 µm
41.1 nm
35.0
30.0
25.0
20.0
15.0
10.0
4.2
a

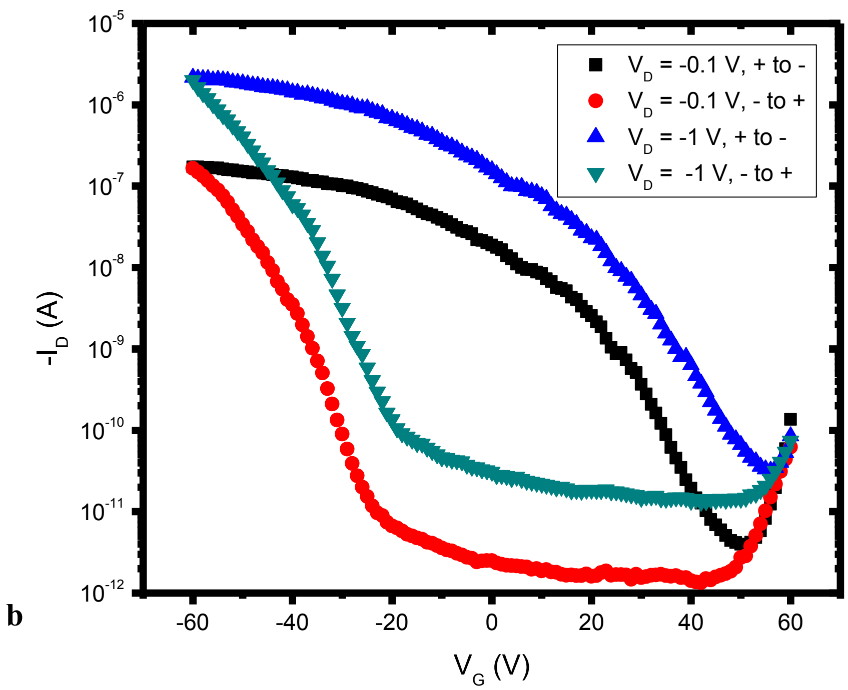

b
-I_D (A)
V_G (V)
V_D = -0.1 V, + to -
V_D = -0.1 V, - to +
V_D = -1 V, + to -
V_D = -1 V, - to +

Figure 3.2

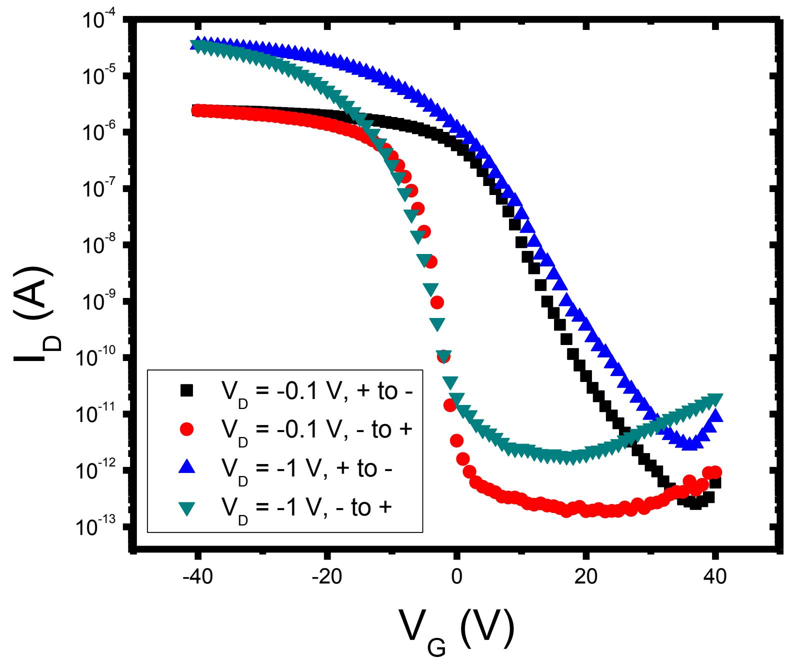

10^-4
10^-5
10^-6
10^-7
10^-8
10^-9
10^-10
10^-11
10^-12
10^-13
I_D (A)
V_D = -0.1 V, + to -
V_D = -0.1 V, - to +
V_D = -1 V, + to -
V_D = -1 V, - to +
-40
-20
0
20
40
V_G (V)

c

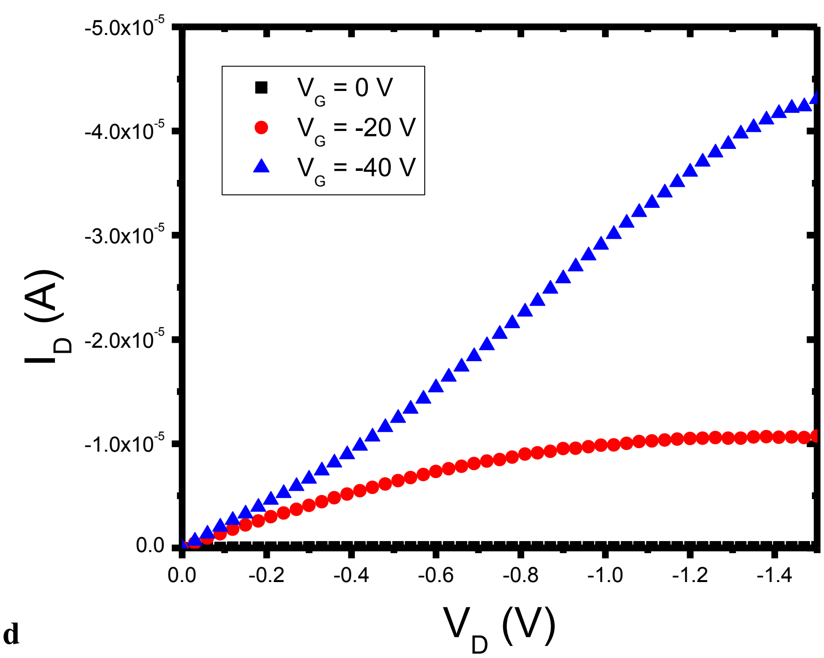

-5.0x10^-5
-4.0x10^-5
-3.0x10^-5
-2.0x10^-5
-1.0x10^-5
0.0
I_D (A)
V_G = 0 V
V_G = -20 V
V_G = -40 V
0.0
-0.2
-0.4
-0.6
-0.8
-1.0
-1.2
-1.4
V_D (V)

d

Figure 3.2

Figure 3.2. Electrical characterization of field effect transistors fabricated from WSe_2 flakes with Pd contacts. (a) AFM map of a device fabricated from a ~9 nm thick WSe_2 flake. (b)Ambient I_D-V_G characteristics plotted logarithmically at two different source drain voltages V_D = -0.1 V and V_D = -1 V. Large hysteresis is observed. The same device is measured under vacuum conditions of 10^{-5} mbar. (c) The I_D-V_G characteristics are shown with reduced hysteresis and improved on/off ratio, while (d) displays the I_D-V_D characteristics, including the onset of saturation in the device.

Variations in properties of were measured across different fabricated devices. For example, **Figure 3.3** shows an ambipolar device with both n and p-type conduction, measured in a vacuum pressure of ~10^{-5} mbar. The V_D = -0.1 V current on/off ratio was approximated to be ~10^8 and ~10^5 at the negative and positive gate biases, respectively. The asymmetry has been reported to be potentially caused by different thresholds for electron and hole type operation, as well as the negative polarity of V_D [30]. The variations in conduction methods across devices has been previously reported in MoS_2 and attributed to intrinsic defects [31]. A ~20 V hysteresis is observed in the I_D-V_G characteristic. The linear I_D-V_D plots of both the positive and negative V_G biases are shown in **Figure 3.3b-c**. Due to the magnitudes of difference in the currents, I_D for V_G = 60 V and – 60 V are observed in the plots. The log(I_D) vs. V_D plot is thus shown in the insets. Current saturation is only observed at negative back gate voltage The noise level of the Agilent 4156C used to measure the current was around 10^{-14}~10^{-13} A.

a

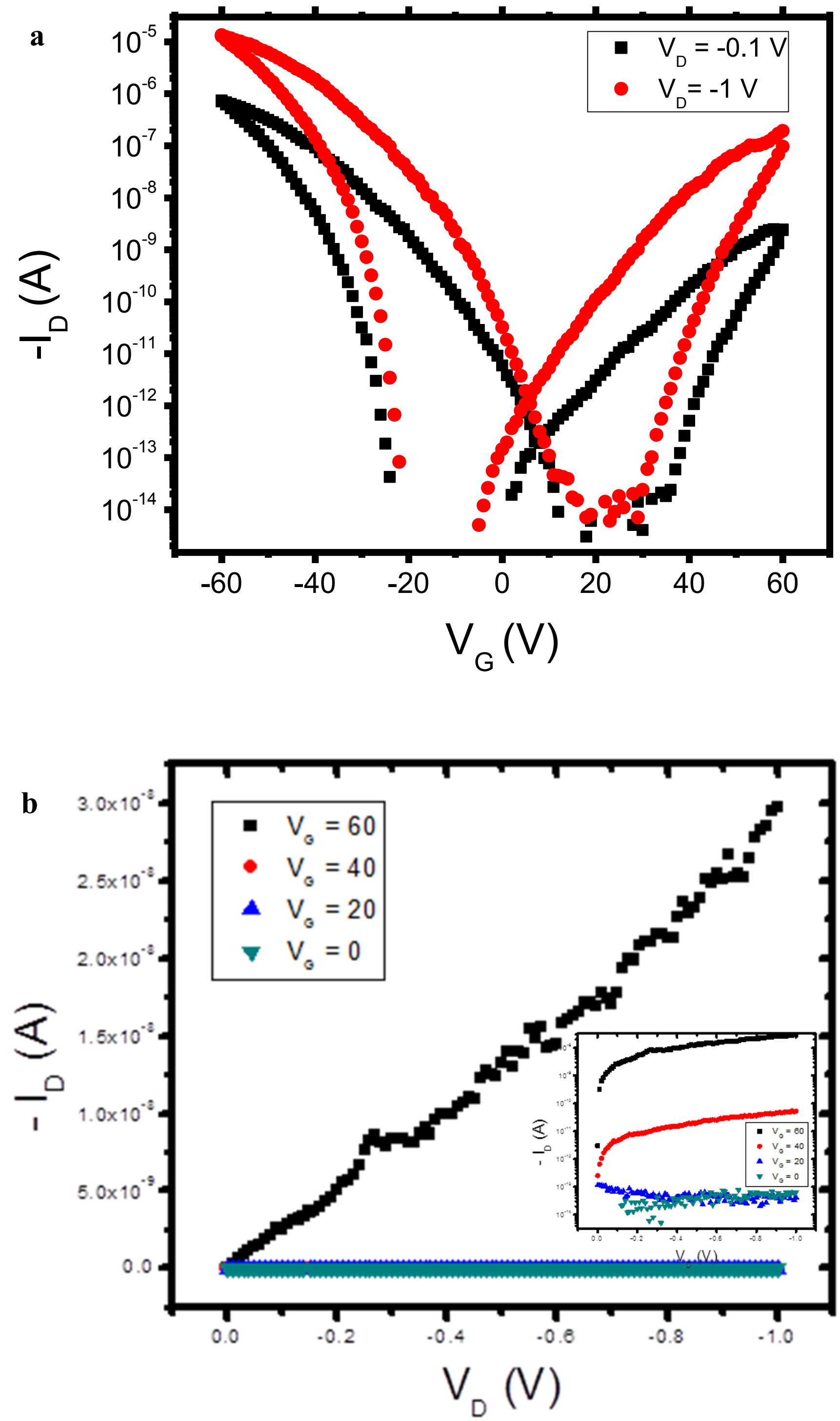

b

Figure 3.3.

c

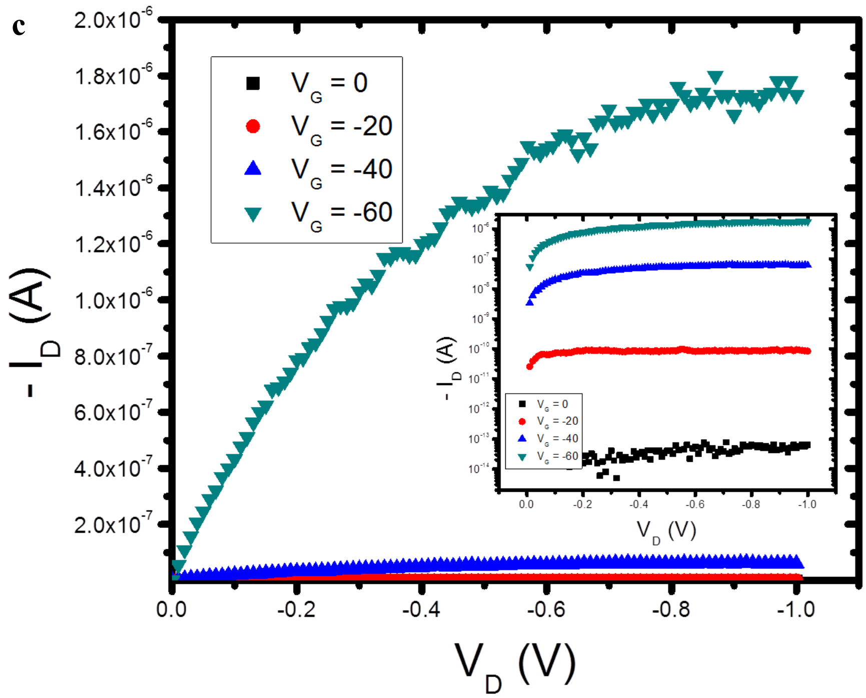

Figure 3.3. Electrical measurements of ambipolar field effect transistors fabricated from WSe_2 flakes with Pd contacts. (a) I_D-V_G characteristics plotted logarithmically at two different source drain voltages V_D = -0.1 V and V_D = -1 V. The I_D-V_D characteristics at (b) positive and (c) negative V_G show the conduction properties for electrons and holes, respectively. The insets of (b) and (c) plot I_D logarithmically against V_D.

Chapter 4: Thermal Oxidation of WSe_2

WSe_2 were found to thermally oxidize under certain conditions. This chapter outlines the process of oxidation and characterizes the material before and after oxidation. The oxidation process produces lateral structures of WSe_2 and WO_3.

4.1 SYNTHESIS

Exfoliated WSe_2 flakes could be oxidized in an ambient or oxygen atmosphere at ~400 ºC. The sequence is captured with a 20x optical microscope in **Figure 4.1**, with the assistance of Avinash Nayak and Prof. Jung-fu Lin. The oxidation begins at the edge of the WSe_2 flakes, and a clear color contrast is observed between the center of the flake and the outer ring. With time, the oxide spreads inwards until the entire flake becomes oxidized. The resulting oxide is referred to as WO_x in this chapter.

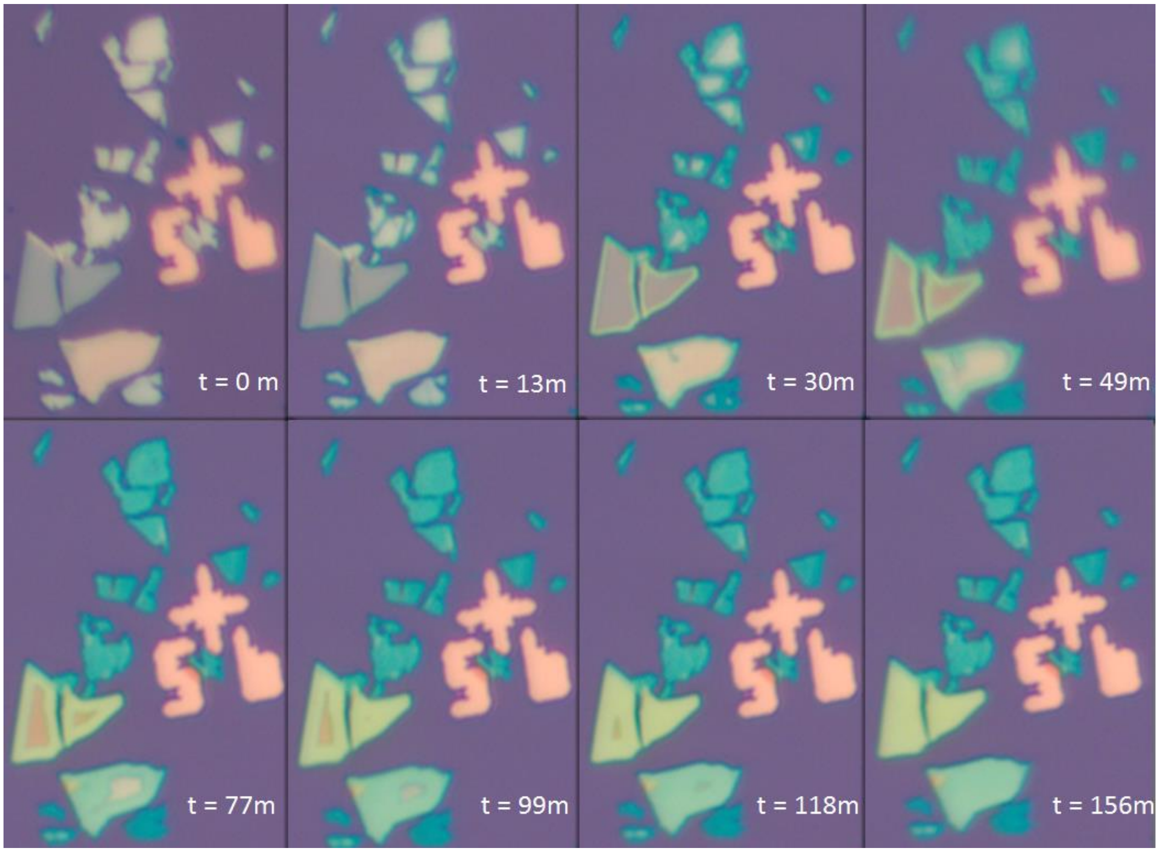

Figure 4.1. Time-lapsed image of WSe_2 flakes oxidized at 400 ºC. Oxidation is observed to start at the edge of the flake and move inwards. Taken with 20x objective.

4.2 Characterization

As shown in the optical images in **Figure 4.1**, oxidation takes place from the edge in towards the center, changing the color of the flakes as it occurs. **Figure 4.2** characterizes the process. **Figure 4.2a** displays the AFM image (obtained from collaborations with Prof. Keji Lai and Yingnan Liu) of original bulk WSe_2 flake before oxidization, in which red arrows outline the original defects. Oxidation along these defects as well as the flake edge is observed (**Figure 4.2b**). These oxidized bands are also visually observed in **Figure 4.2c**.

The atomic composition of the oxidized flake is obtained through time of flight secondary ion mass spectrometry (ToFSIMS, **Figure 4.2d**) with the assistance of Harry Chou. The figure shows the compiled image after 20 seconds sputter time, the composition at the surface of these oxidized bands are composed of W and O, and little to no Se signature is detected. The lack of Se at the outer edge may be due to the formation of SeO_2 in the process, which sublimes at 350 ºC. However, in the bulk material below the surface (**Figure 4.2e**), only the edge is oxidized, suggesting that the oxidation due to the surface defects is only limited to the topmost layers, and edge oxidation is the primary method of oxidation lower layers. MIM measurements can also be used to characterize the process, as shown in the imaginary maps before and after oxidation (**Figure 4.2f-g**, in collaboration with Prof. Keji Lai and Yingnan Liu**). Figure 4.2g** shows the oxidized bands as having higher conductivity than the unoxidized WSe_2.

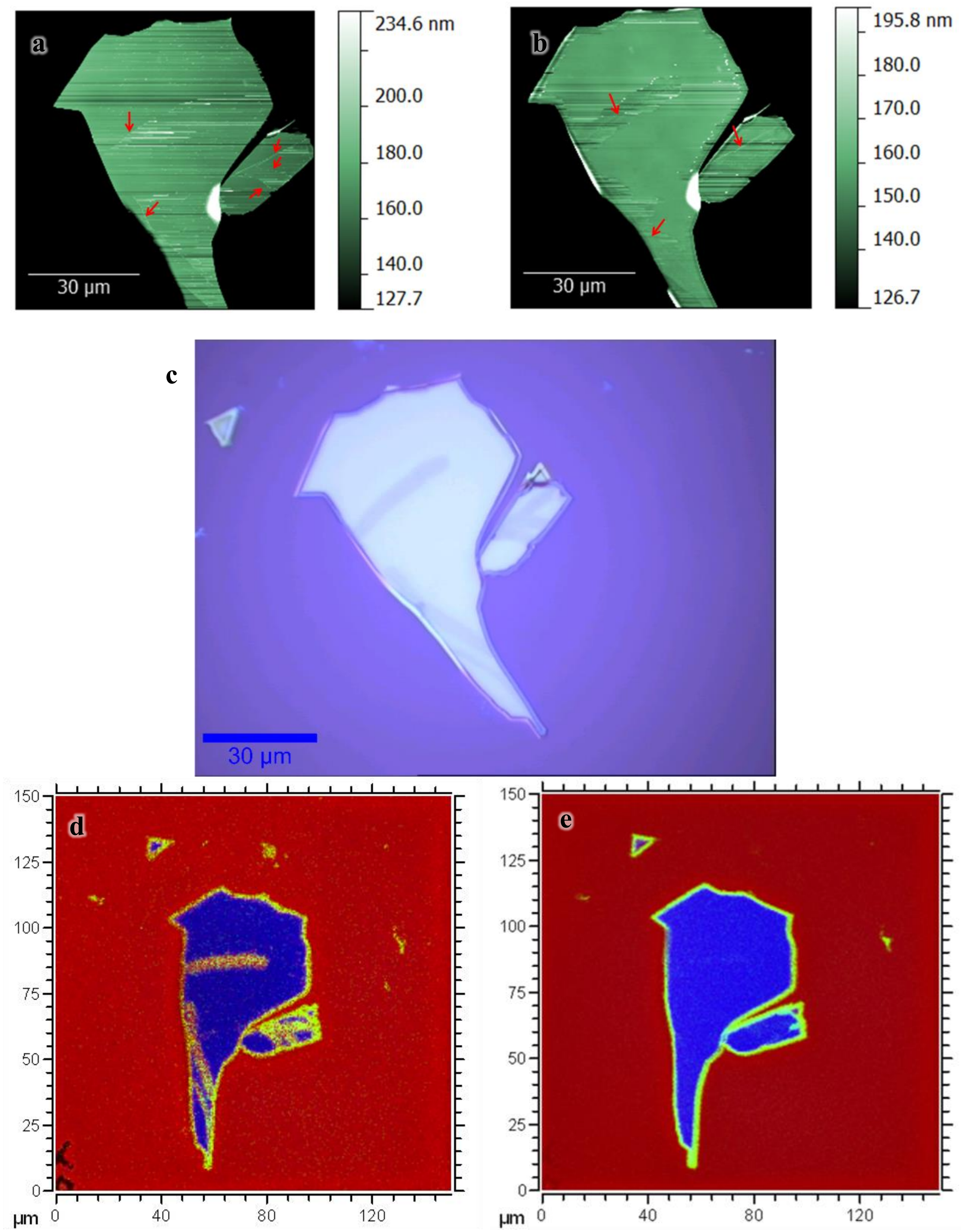
a
234.6 nm
200.0
180.0
160.0
140.0
127.7
30 µm
b
195.8 nm
180.0
170.0
160.0
150.0
140.0
126.7
30 µm
c
30 µm
d
e
µm
0
40
80
120
25
50
75
100
125
150

Figure 4.2.

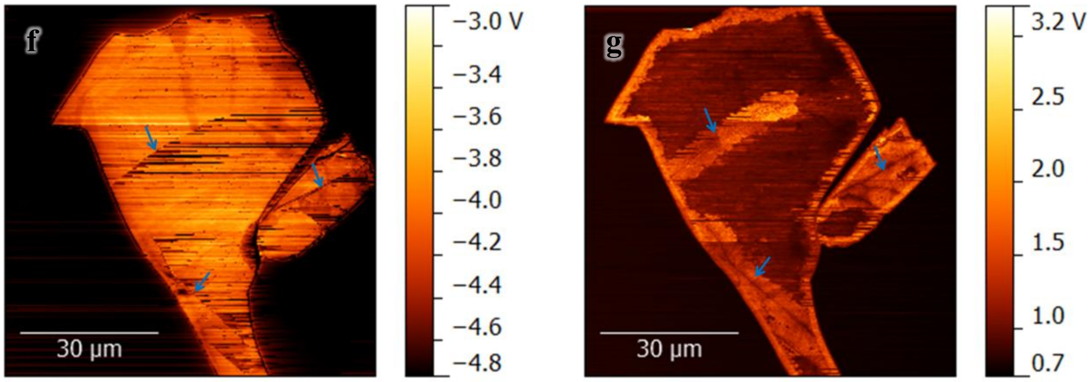

Figure 4.2. Characterizations of a WSe_2 flake before and after oxidation. (a) AFM image of a bulk WSe_2 flake before oxidation. Arrows mark the defects in the flake. (b) AFM image of the same flake after oxidation, arrows mark the original defects prior to oxidation. A band of oxidation is observed around these defects as well as the edges. (c) Optical image of the same flake post oxidation. The bands shown in the AFM image are visible here due to the optical contrast. (d) ToFSIMS map of oxidized WSe_2 flake after first 20 seconds of sputtering. The red corresponds to O^- ions, blue to Se^-, and the green to WO_2^-. (e) Accumulated ToFSIMS map the oxidized WSe_2 scan. The bands in (d) are not observed in (e). (f-g) Contrast adjusted imaginary MIM maps for WSe_2 before (f) and after (g) oxidation, defects are outlined by blue arrows. The bands are more easily observed through MIM than AFM due to a higher contrast from the surrounding WSe_2.

Raman spectra in **Figure 4.3a** shows a comparison of the WSe_2 flake before and after oxidation, and WO_3 powder for reference. After oxidation, four distinct Raman modes are observed in the spectrum at ~131 cm^{-1}, ~268 cm^{-1}, ~713 cm^{-1}, and ~805 cm^{-1}, which correspond well with the Raman modes observed in the WO_3 powder as well as the ~130 cm^{-1}, ~271cm^{-1}, ~711cm^{-1}, and ~808 cm^{-1} modes of monoclinic (V) and triclinic (VI) WO_3 reported in literature [32-34]. In the oxidized WSe_2, the ~130 cm^{-1} mode has been previously attributed to O-O deformations and the 271 cm^{-1} mode to W-O deformations, whereas the other two modes have been assigned to W-O/O-W-O stretching/vibrational modes in the WO_6 octahedral units [32, 34]. A summed intensity map of the 131 cm^{-1} peak can be seen in **Figure 4.3b**, which outlines the oxidized regions.

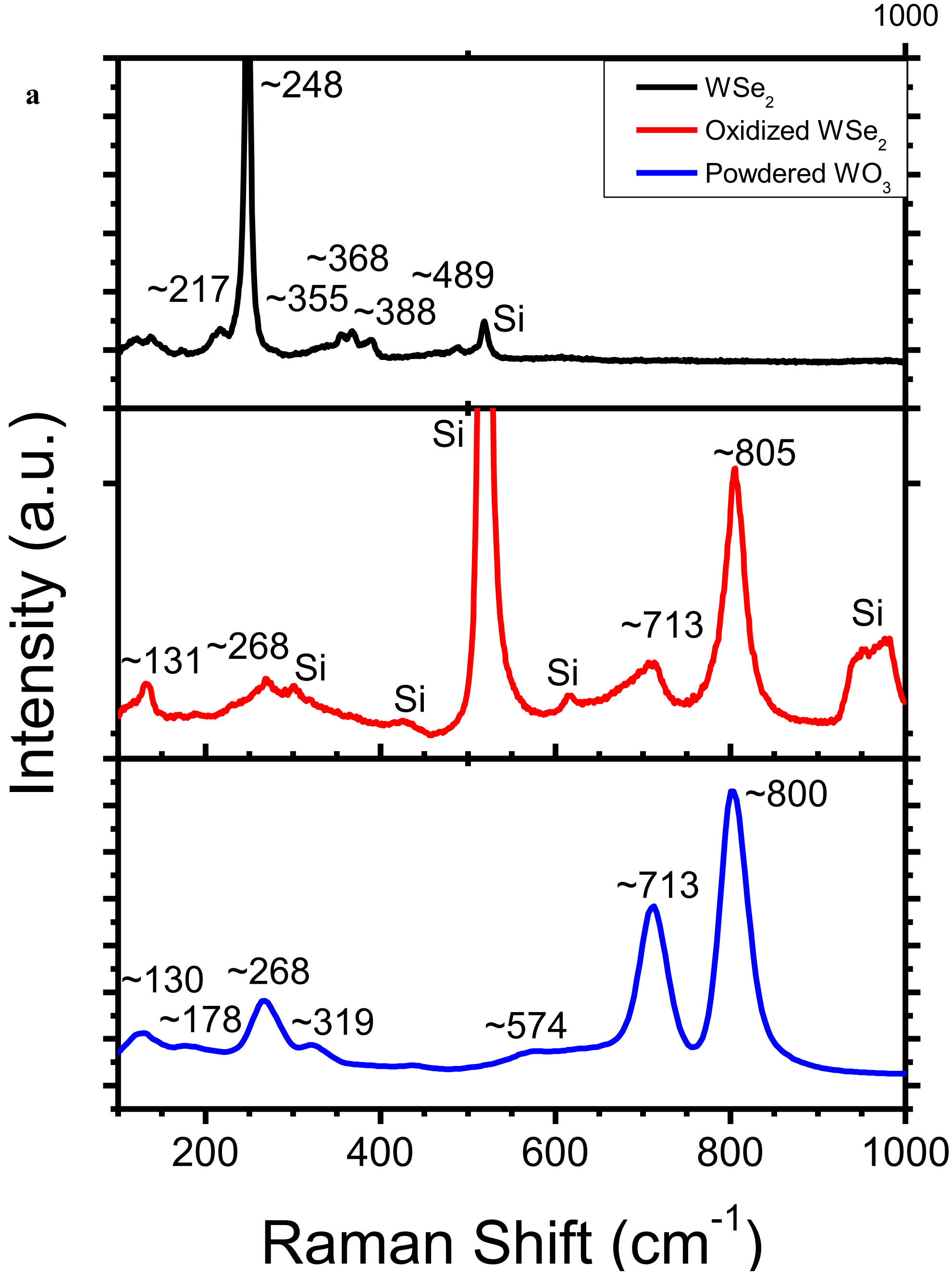
a
1000
WSe2
Oxidized WSe2
Powdered WO3
~248
~217
~368
~355
~388
~489
Si
Si
~805
~131
~268
Si
Si
Si
~713
Si
~800
~713
~130
~268
~178
~319
~574
Intensity (a.u.)
200
400
600
800
1000
Raman Shift (cm-1)

Figure 4.3.

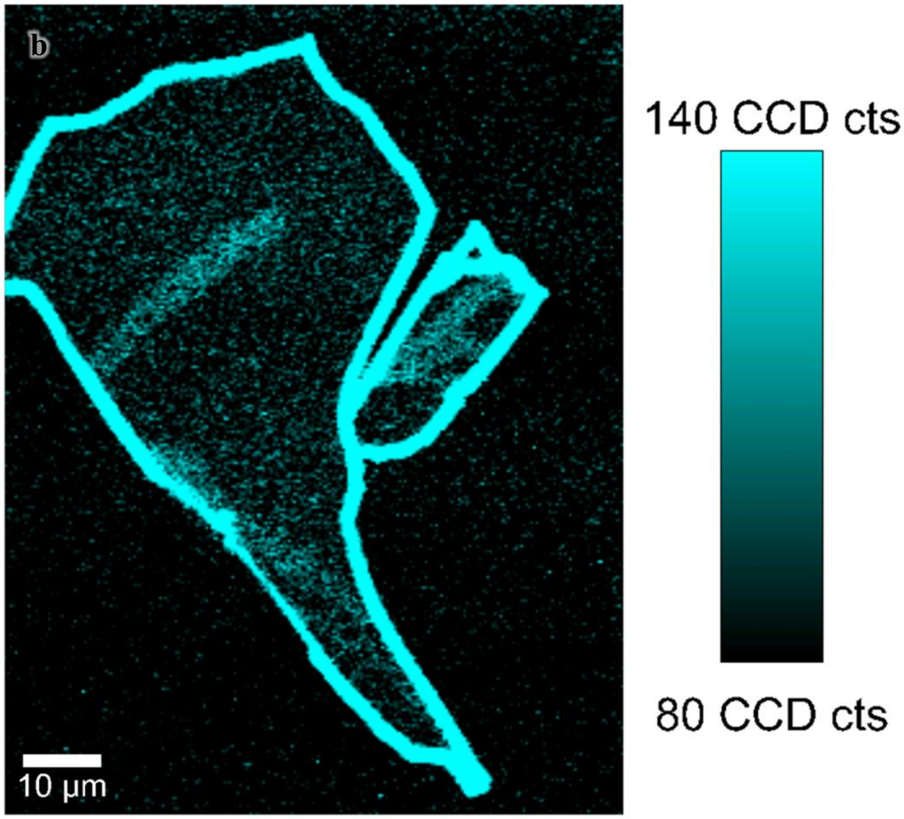

Figure 4.3. Raman characterization of oxidized WSe_2. (a) Raman spectra of unoxidized WSe_2, oxidized WSe_2, and WO_3 powder, from top to bottom. Silicon peaks are as labeled. The oxidized WSe_2 portion retains none of the original signature, and exhibits four modes resembling that of WO_3, which can be identified as Raman modes active in monoclinic (V) and triclinic (VI) WO_3. (b) Raman intensity map summed over the 130 cm^{-1} peak, the bright regions corresponds to the oxidized regions, as characterized in prior figures.

Transmission electron microscopy (TEM) was used to study the details of the oxidized samples, as shown in **Figure 4.4**, with the assistance of Dr. Karalee Jarvis and Avinash Nayak. It is observed from the mass contrast in the center of the oxidized flake (**Figure4.4a**), that the layered structures of WSe_2 are left intact. At the junction between WSe_2 and WO_x, (**Figure 4.4b)**, there is no clear-cut heterojunction. Instead, WSe_2 is observed (towards the bottom of the image) along with the lattice fringes of WO_x, the two distinguished by the lattice spacings, as shown in **Figure 4.4c**. The WSe_2 interlayer distance is measured to be ~ 0.7 nm while the fringes in the WO_x lattice are ~0.35 nm. Due to the polycrystalline nature of WO_x, different lattice fringes are observed, as shown in **Figure 4.4d**. The directions of the fringes are outlined by the parallel lines.

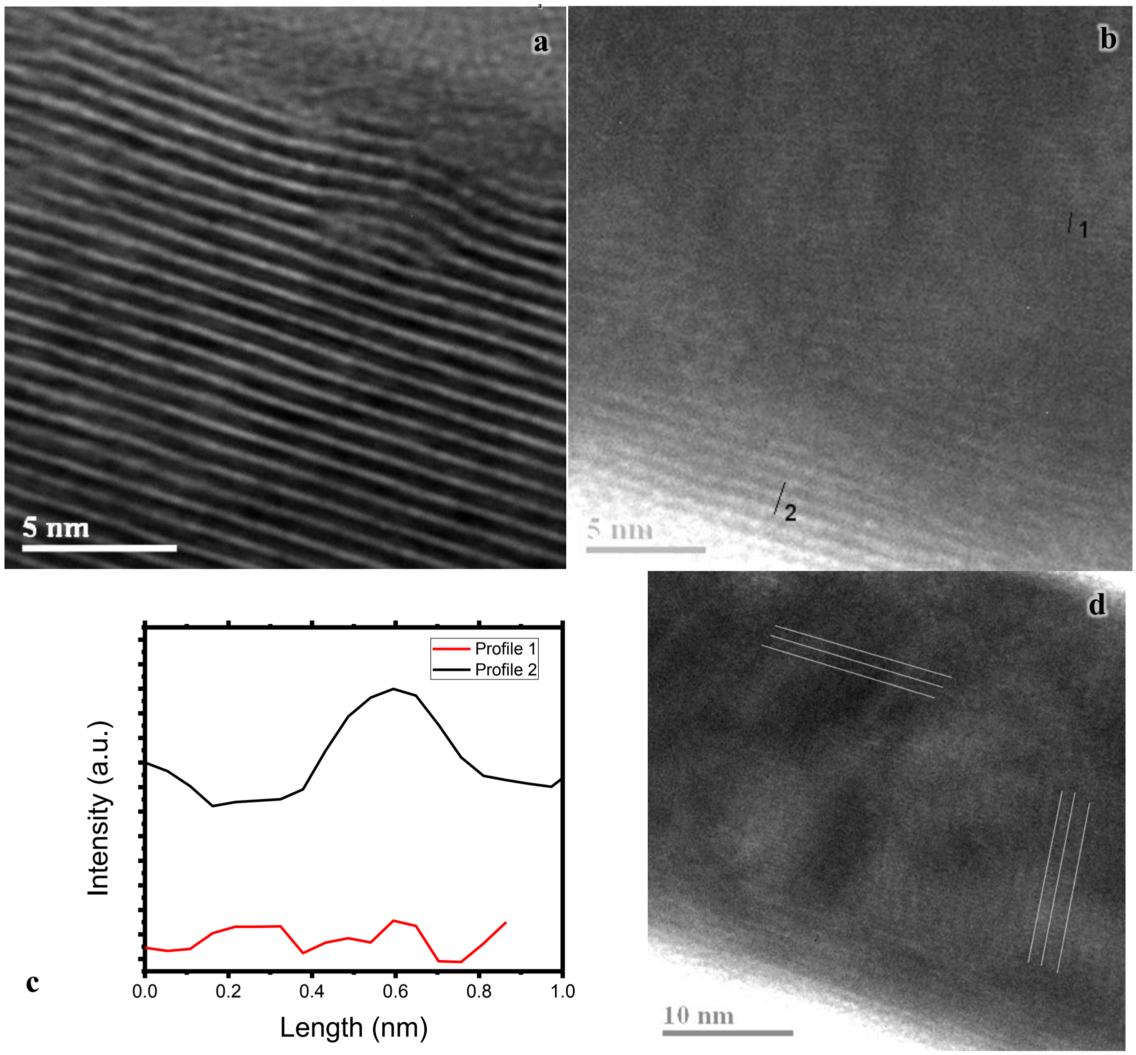

Figure 4.4. TEM characterization of oxidized WSe_2. (a) TEM image of unoxidized area, the lattice fringes of WSe_2 are clearly seen. (b) TEM image of both the WSe_2 (bottom of the image) as well as the WO_x(top of the image), the profiles of which are seen in (c). The profiles show that the interlayer distance of the WSe_2 to be ~0.7 nm whereas the interfringe distance in the WO_x is ~0.35 nm. (d) TEM image of the oxidized region showing the different lattice fringes of the crystals, as outlined by the parallel white lines. These fringes correspond to different planes in the crystals, suggesting that the region is polycrystalline.

Previously in **Figure 4.2**, the MIM map showed for the large flake that the conductivity was higher for the oxidized samples. However, for the smaller flakes, where more of the flake is oxidized, this is not the case. **Figure 4.5a** and **Figure 4.5b** shows the AFM topography image for a WSe_2 flake before and after oxidation. In the center the flake thickness increases from 30 nm to 31 nm whereas at the edge, a decrease in thickness occurs instead. The decrease at the edge of the flake is attributed to the lack of the large distance van der Waals gaps in the WO_x lattice. The slight thickness increase in the center is possibly due to the formation of surface oxides in the uppermost layers, while the van der Waals gap separation is still intact in the WSe_2 layers below. From the imaginary MIM map shown in **Figure 4.5c** and **Figure 4.5d**, the edge oxide shows a decrease in conductivity from the WSe_2, but also a ring of a higher conductivity material closer to the center in the slightly larger flake. This is differs from the larger flake in **Figure 4.3**, which only shows the higher conductivity edge (the very edge, however, shows an almost unnoticeable drop in conductivity). This is possibly due to the oxidation starting from the edge towards the center, and the oxide at the edge has had the time to completely oxidize and reorder, whereas the near the oxidation front the material may still contain O vacancies or Se impurities, as it has not completely oxidized. The lack of reordering may explain how the higher conductivity region still retains the original thickness of the flake (and even slightly thicker) (shown in **Figure 4.5b**), as well as the Raman signature of WSe_2.

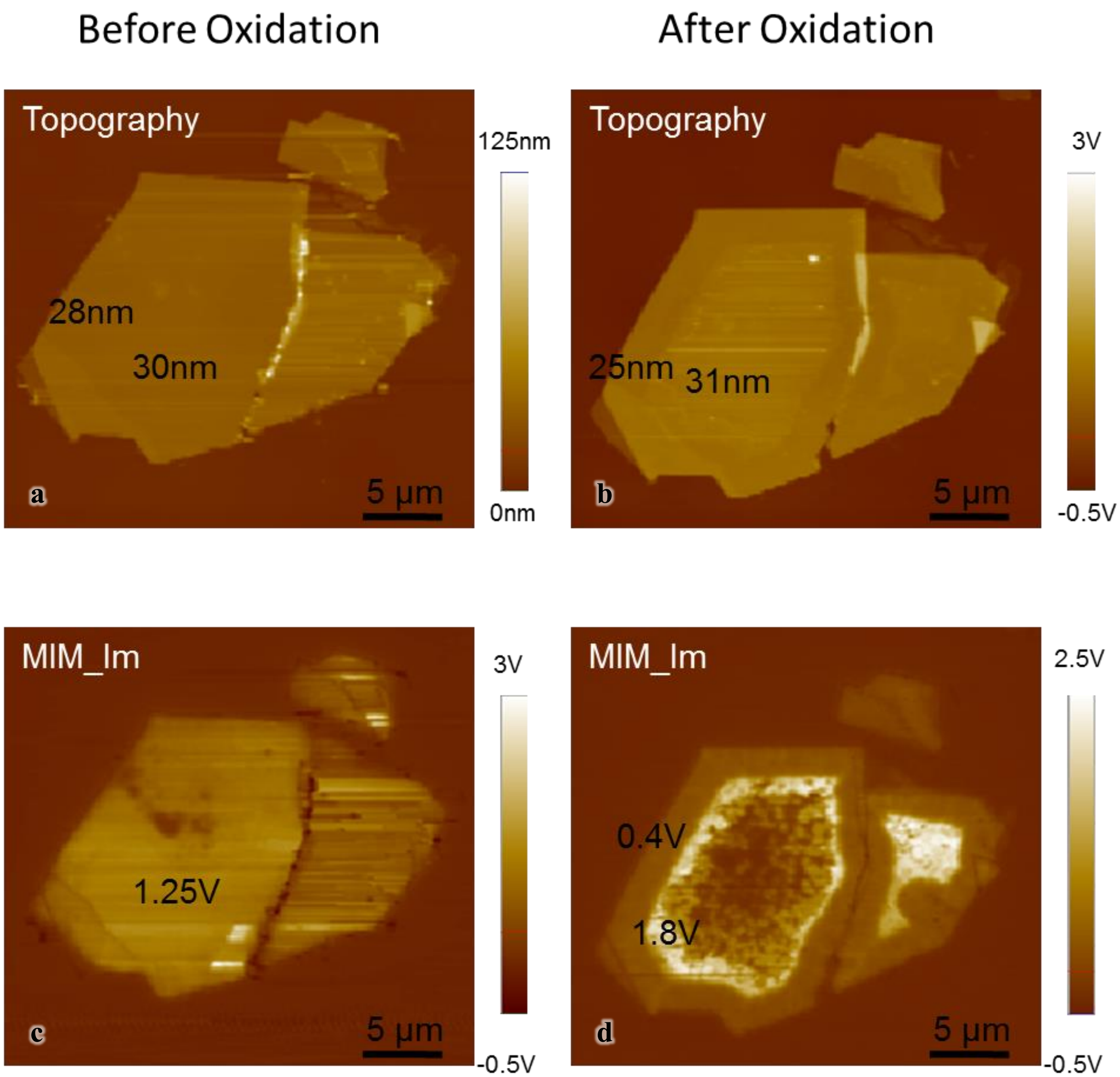

Figure 4.5. AFM and MIM characterization of oxidized WSe_2. AFM topography images (a) before and (b) after oxidation. A thickness decrease in the oxidized edge is observed, whereas in the center there is a slight increase in thickness, possibly due to surface oxidation. Imaginary MIM maps of WSe_2 flakes (c) before and (d) after oxidation. A decrease in conductivity is seen at the outer edge, whereas there is a ring of higher conductivity around the center in the larger flake.

Chapter 5: Laser Oxidation of WSe_2

In addition to thermal oxidation, it was also found that it is possible to selectively oxidize areas of WSe_2 using a laser at room temperature. The details of the process and the subsequent characterizations are outlined in this chapter.

5.1 SYNTHESIS

A 488 nm laser was used with a WiTec Alpha 300 micro-Raman imaging system to oxidize the exfoliated WSe_2 flakes. Setting the objective to 100x (~250 nm spot diameter) and the laser to ~11 mW output, the power density was calculated to be ~ 2.24 $\times 10^{-4}$ mW/nm^2. Using this method, it is possible to selectively oxidize areas of interest, presumably through localized heating of the WSe_2 surface. The resulting oxide is referred to as WOx in this section.

Due to the discrete movement of the system stage, lines of oxidation are observed. **Figure 5.1a** shows the AFM map of a WSe_2 flake that was first scanned horizontally and then vertically (bottom of map is unscanned). Trenches are due to the non-uniform oxidation from discrete stage movement. Also, scanning in both directions does not create a checkered pattern. Instead, the region that was scanned horizontally does not appear to experience further oxidation in the subsequent vertical scan. The non-uniformity problem can be alleviated through the changing scan settings via the pixel density. **Figure 5.1a-e** shows the AFM image of scans taken with pixel densities of 4, 5, 6, 7, and 8 pixels/um, respectively. The oxidized areas (top of images) are shown to become more uniform with higher pixel densities, at the expense of longer scanning times. At 8 pixels/um, the trenches are only observed at the edges, where the resetting of scan (from +y to -y for every line) direction may have led to the uneven heating in these areas. This problem is solved by alternating the scan direction between every line of the scan, as shown in **Figure 5.1e**, which shows the result of a 8 pixel/um scan using alternating horizontal scan directions. The profile across the WSe_2\WOx junction is shown in **Figure 5.1f**, and the oxide is shown to have depressed by ~4 nm across the junction (profile in **Figure 5.1g**).

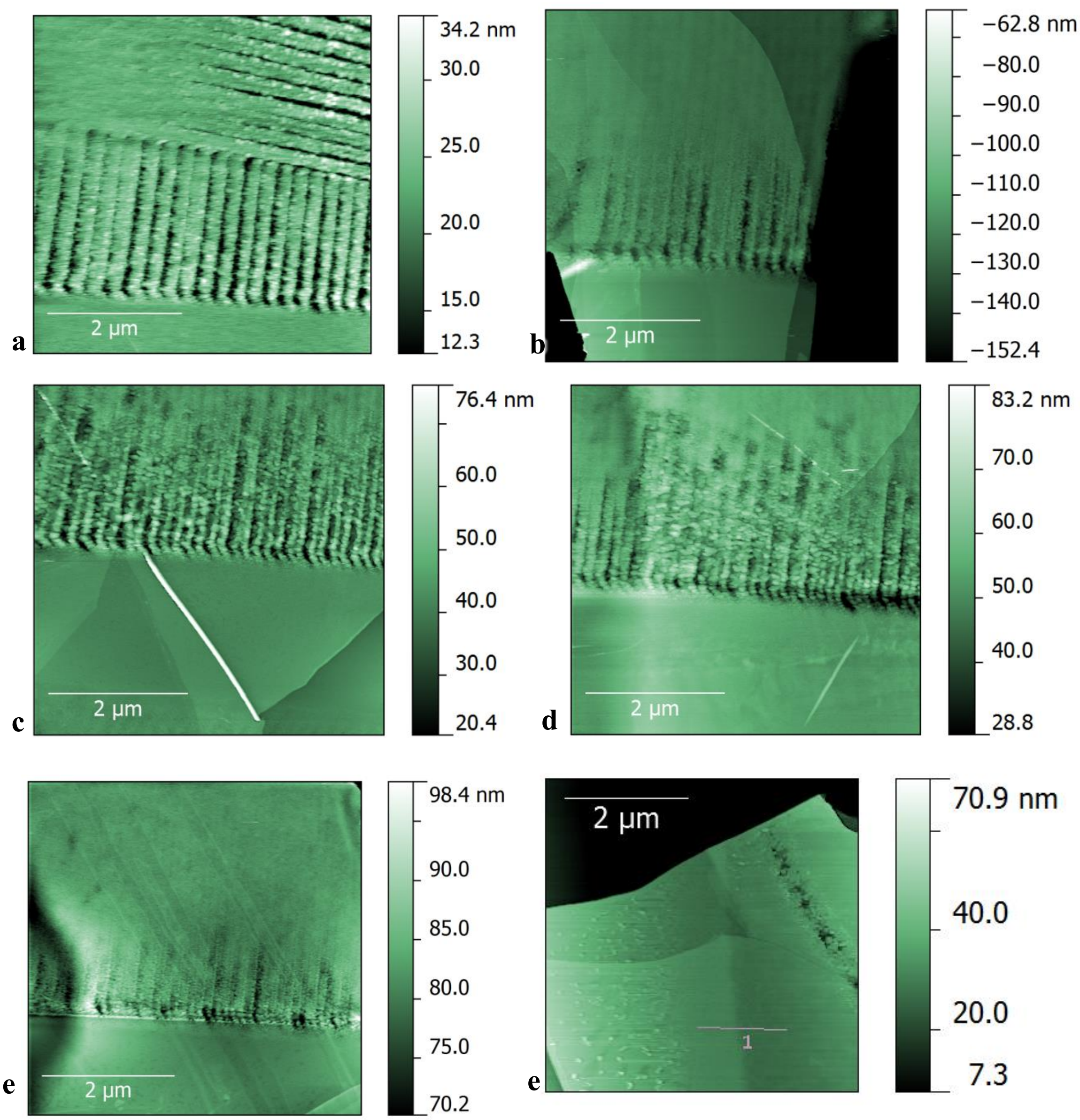

Figure 5.1.

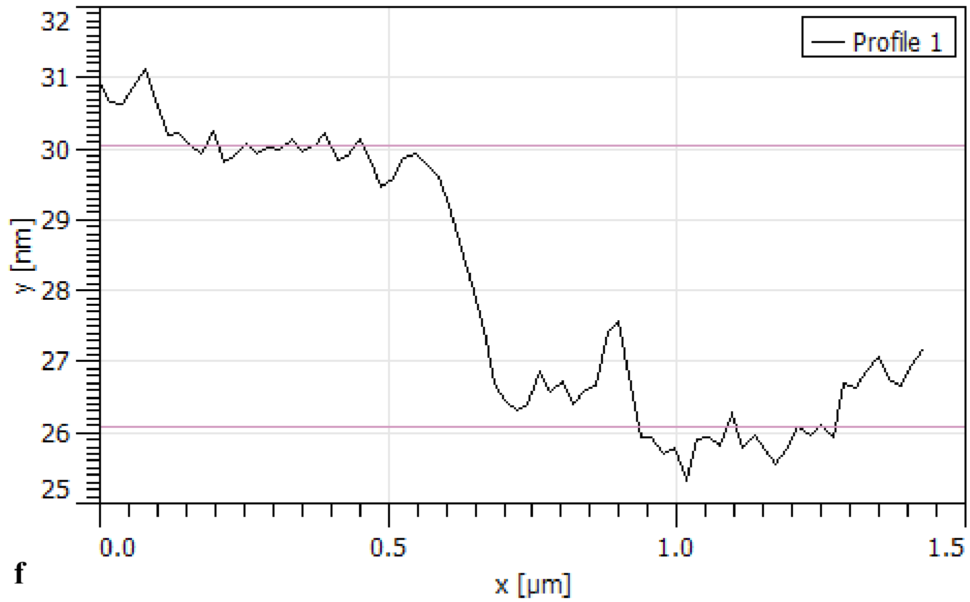

f

Figure 5.1. AFM characterization of laser oxidized WSe_2. (a) AFM map of a WSe_2 flake scanned first horizontally and then vertically at 4 pixels/um. The trenches from the scan are apparent. Additions vertical scans were done at (b) 5 pixels/um, (c) 6 pixels/um, (d) 7 pixels/um, and (e) 8 pixels/um. With increasing pixel density there is greater uniformity. The trenches near the edge of the scan can be removed by alternating the scan direction between lines, as shown in (f). The profile in (f) is shown in (g), where the vertical distance between the two lines is measured to be ~4 nm.

5.2 CHARACTERIZATION

Figure 5.2a shows a ToFSIMS overlay map of two laser-oxidized WSe_2 flakes. The dark blue represents O^-, the light blue WO_2^-, and the red Se^-. In the unoxidized smaller flakes, only Se^- signature was found. For the oxidized flakes, the cross sectional depth profile in **Figure 5.2b** shows that these flakes are not completely oxidized, as Se^- is still detected in the bottom most regions.

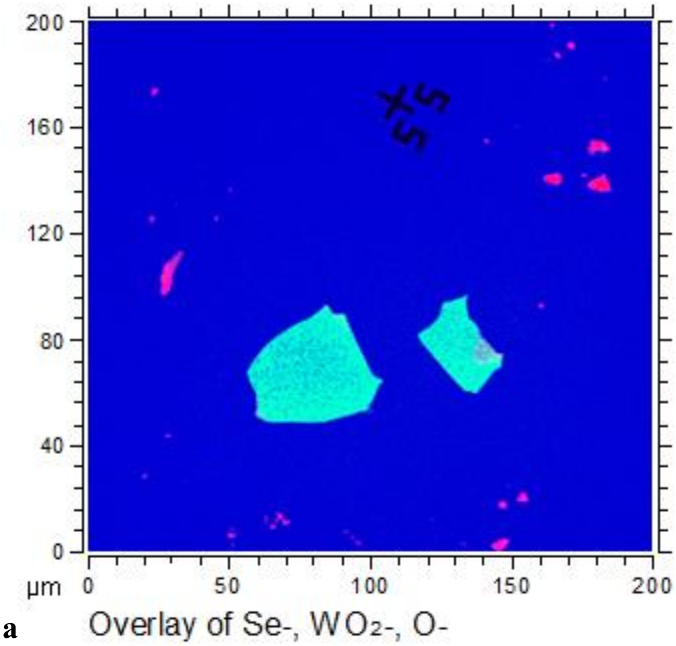

a

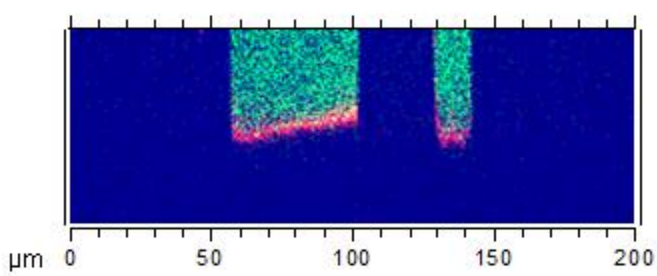

b

Figure 5.2. (a) ToFSIMS map of laser oxidized flakes, showing the selectivity of the oxidation and the elemental composition. The red represents Se^- signature, the blue O^-, and the light blue WO_2^-. (b) X-direction cross sectional depth profile of the two oxidized flakes, showing that the bottom of the flakes still contain Se^- signature.

Raman spectroscopy of oxidized flakes (**Figure 5.3a**) shows both the ~248 cm^{-1} and ~255 cm^{-1} modes of WSe_2 as well as the ~130 cm^{-1}, ~707 cm^{-1}, and 806 cm^{-1} modes of WO_3. The Raman spectrum provides additional evidence that the flakes are not completely oxidized. Raman intensity mapping of a partially oxidized flake over the ~806 cm^{-1} peak is shown in **Figure 5.3b**. The unoxidized half of flake is not apparent in the map. The entire flake is shown in the optical image in **Figure 5.3c**, and the oxidized area is optically distinguishable. The contrast between oxidized and unoxidized regions is observed in both the optical image and the MIM maps, as shown in **Figure 5.4** (In collaboration with Prof Keji Lai and Yingnan Liu). From the MIM results, the oxidized region is shown to have a higher conductivity than the semiconducting WSe2. A stark contrast exists between the two sides of the 15 nm thick flake.

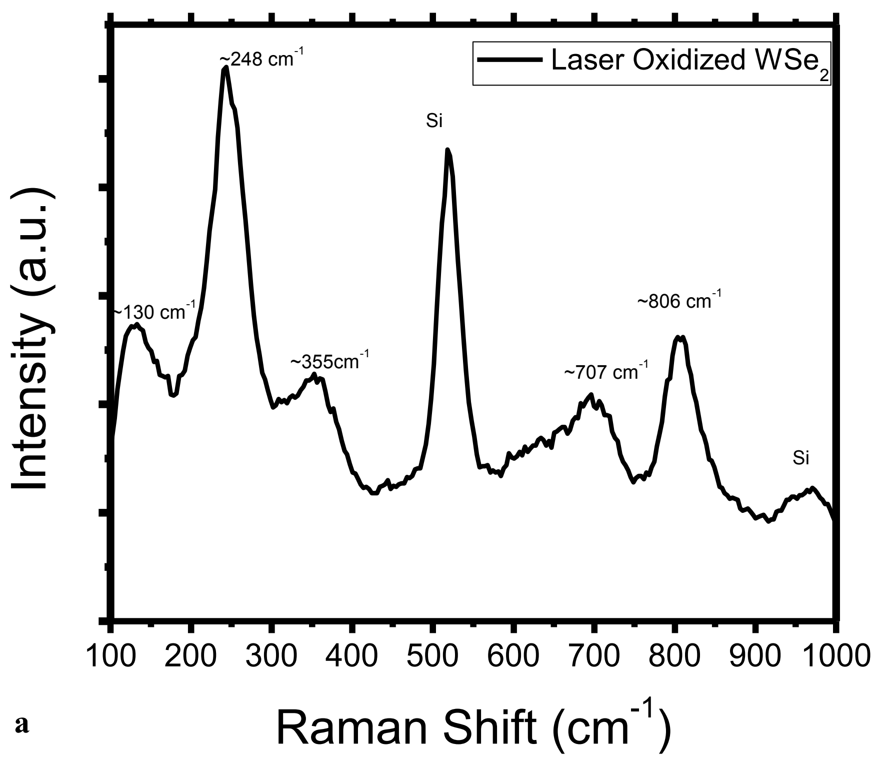

a

Figure 5.3.

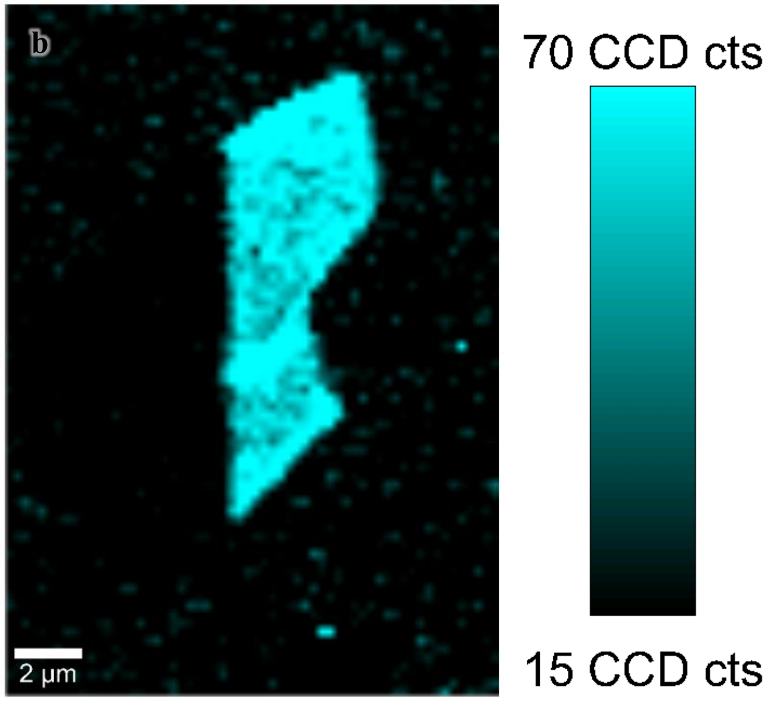

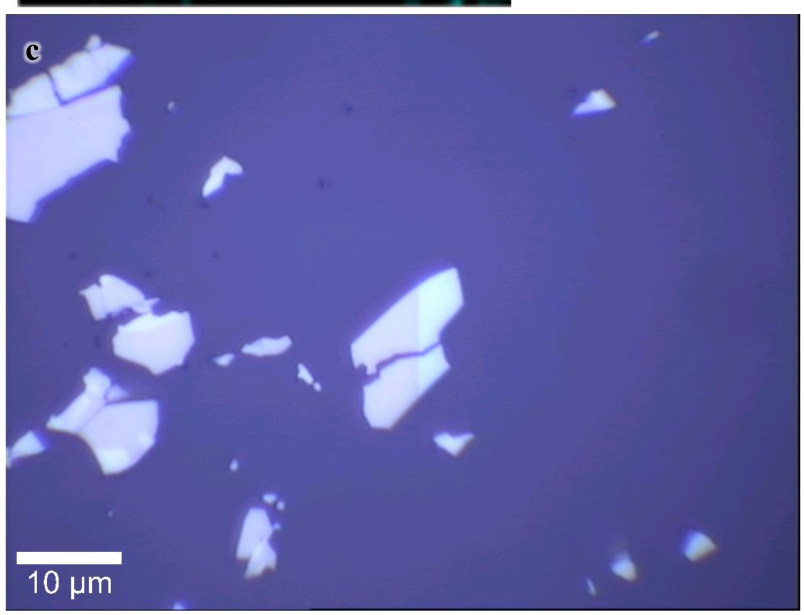

Figure 5.3. (a) Raman spectrum of a typical laser oxidized flake. Both WSe_2 and WO_3 signature are observed. (b) Raman intensity map of the ~806 cm^{-1} mode of a half oxidized flake, the optical image of which is shown in (c) and a slight optical contrast is observed between the two regions.

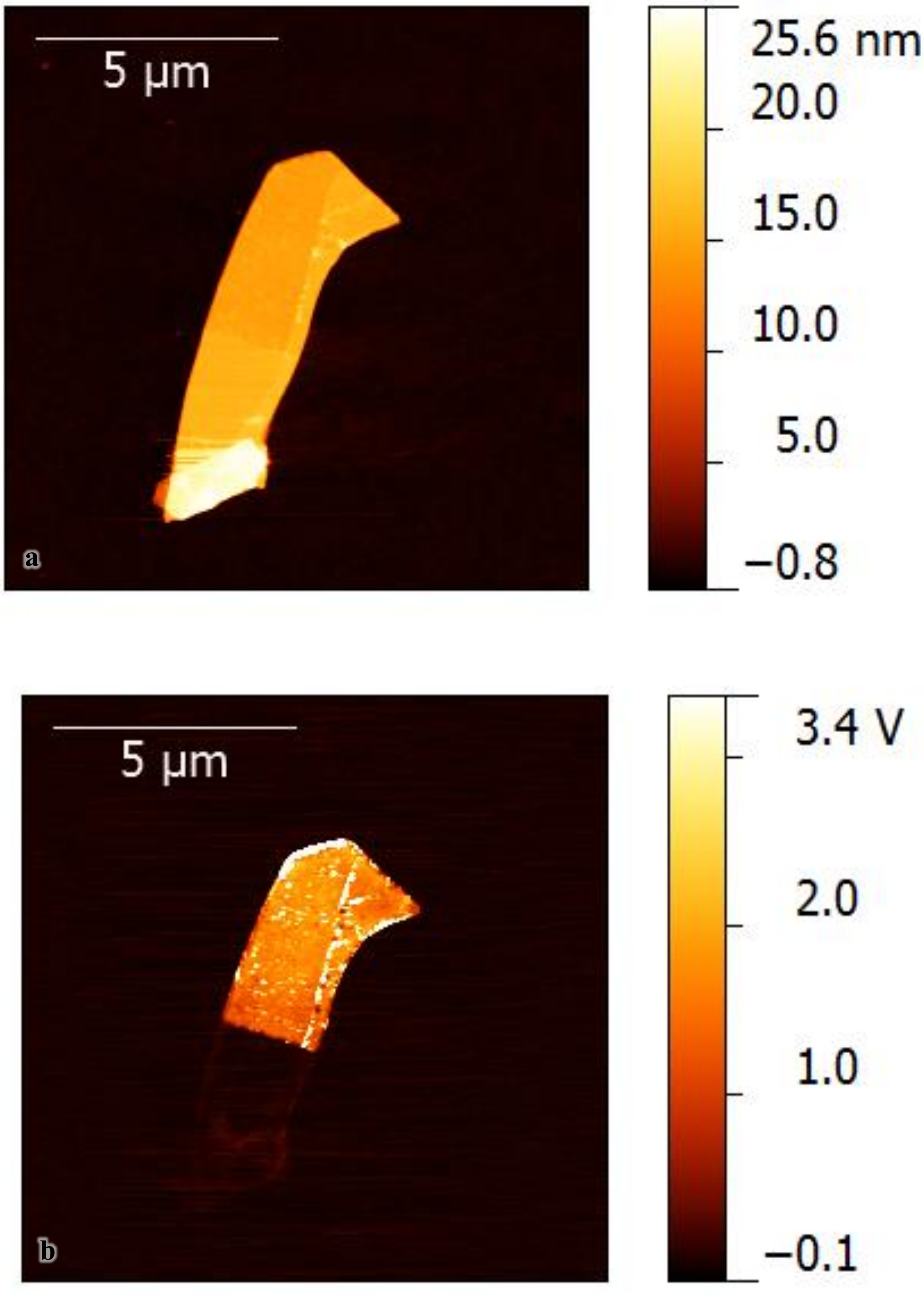

Figure 5.4

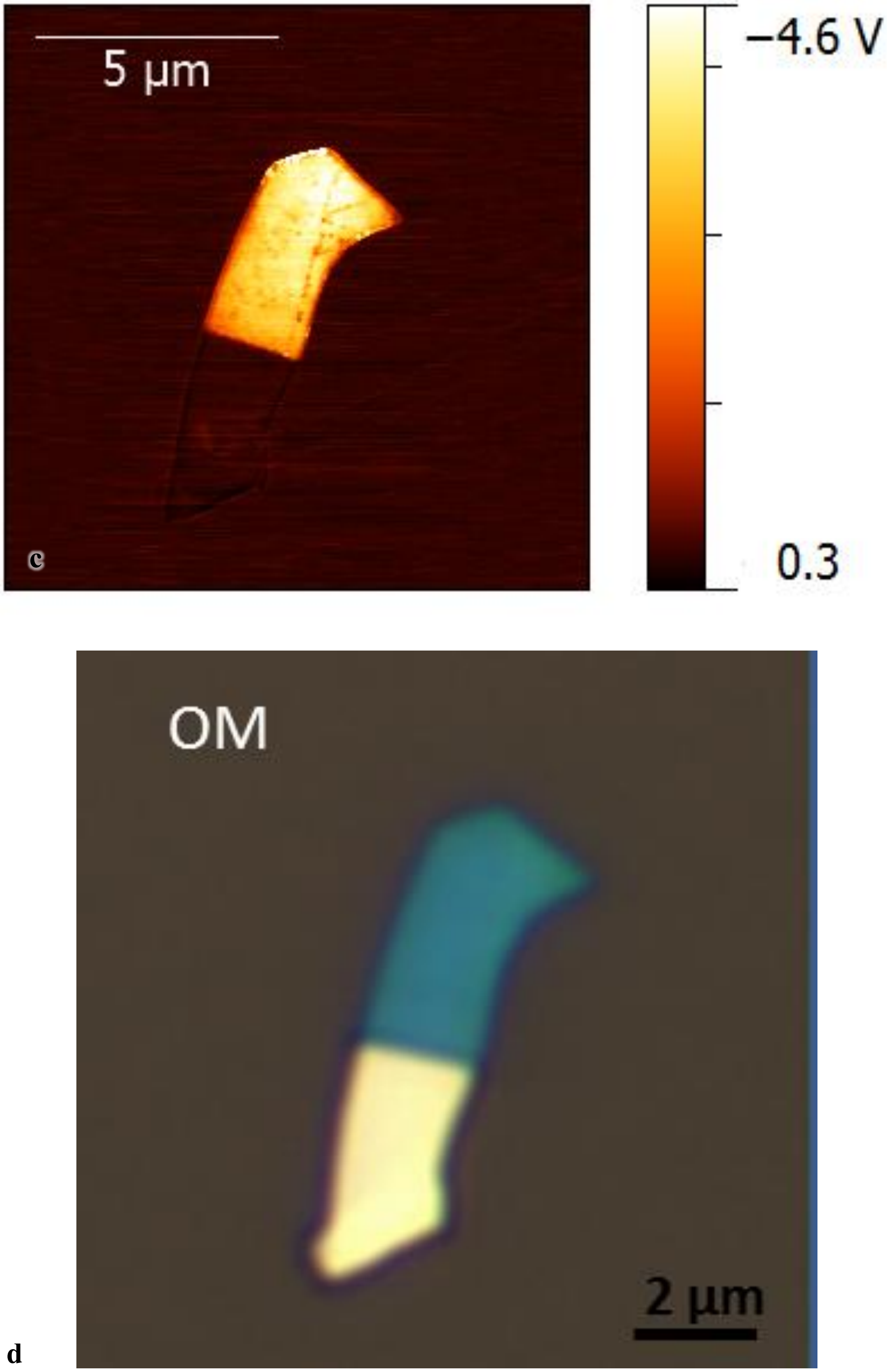

d

Figure 5.4

Figure 5.4. (a) AFM topography map of a WSe_2 flake with the top half laser oxidized. (b) MIM (b) real and (c) imaginary maps of the oxidized flake. (d) Optical image of the flake, the blue region is the oxidized region.

To further investigate the electronic properties of WOx, four point probes were fabricated on each side of the flake (90 nm SiO_2/Si substrate) using electron beam lithography followed by contact deposition and subsequent lift-off (see Chapter 3.1 for more details). The fabricated device is shown in **Figure 5.5** along with the measured four point sheet resistances of WSe_2, WOx, and the WSe_2\WOx junction as a function of applied back gate voltage V_G as well as drain voltage V_D. The device was measured in a vacuum atmosphere of ~10^{-5} mbar The sheet resistance of the WOx was found to be ~4×10^6 Ω/□ at $V_G = 0$ V and high V_D ($|V_D| > 1.5$ V); the sheet resistance of the junction area was found to be ~2×10^8 Ω/□ while WSe_2 was measured at ~10^{10} Ω/□. This result qualitatively matches that of the MIM map, which shows the semiconducting WSe_2 as less conductive when there are no applied gate voltages. However, by biasing V_G, a 10^6~10^8 change is observed in the sheet resistance of WSe_2, depending on the polarity of V_G. When WSe_2 is "on," the resistance of WSe_2 drops below or approaches that of WOx. While WSe_2 experiences significant gate control, sheet resistance across the junction and WOx show little gate control comparatively.

a 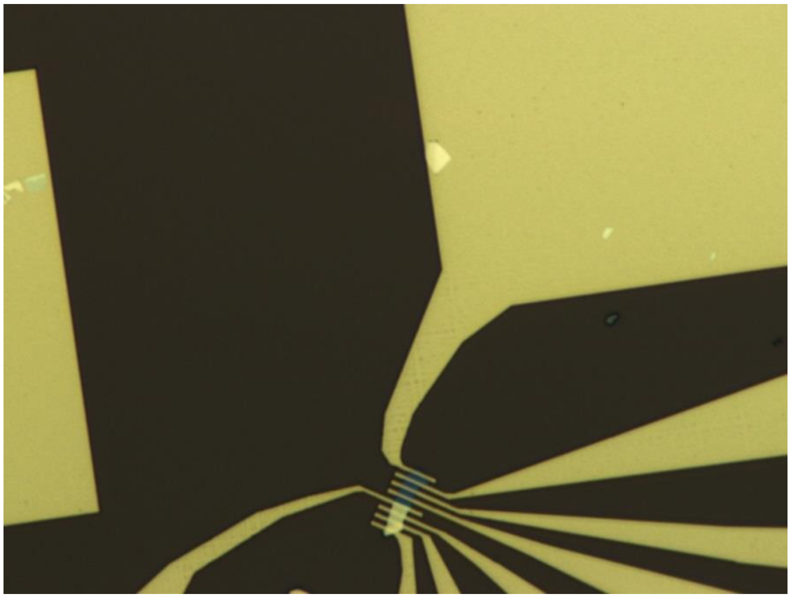

b 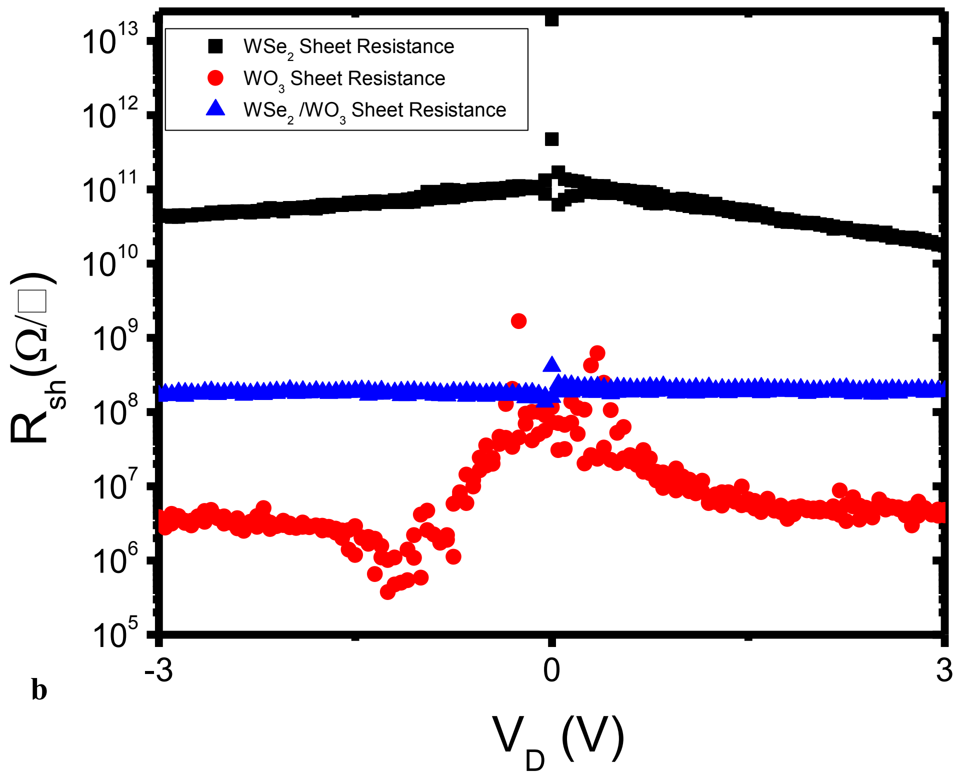
WSe2 Sheet Resistance
WO3 Sheet Resistance
WSe2 /WO3 Sheet Resistance
10^13
10^12
10^11
10^10
10^9
10^8
10^7
10^6
10^5
Rsh(Ω/□)
-3
0
3
VD (V)

Figure 5.5.

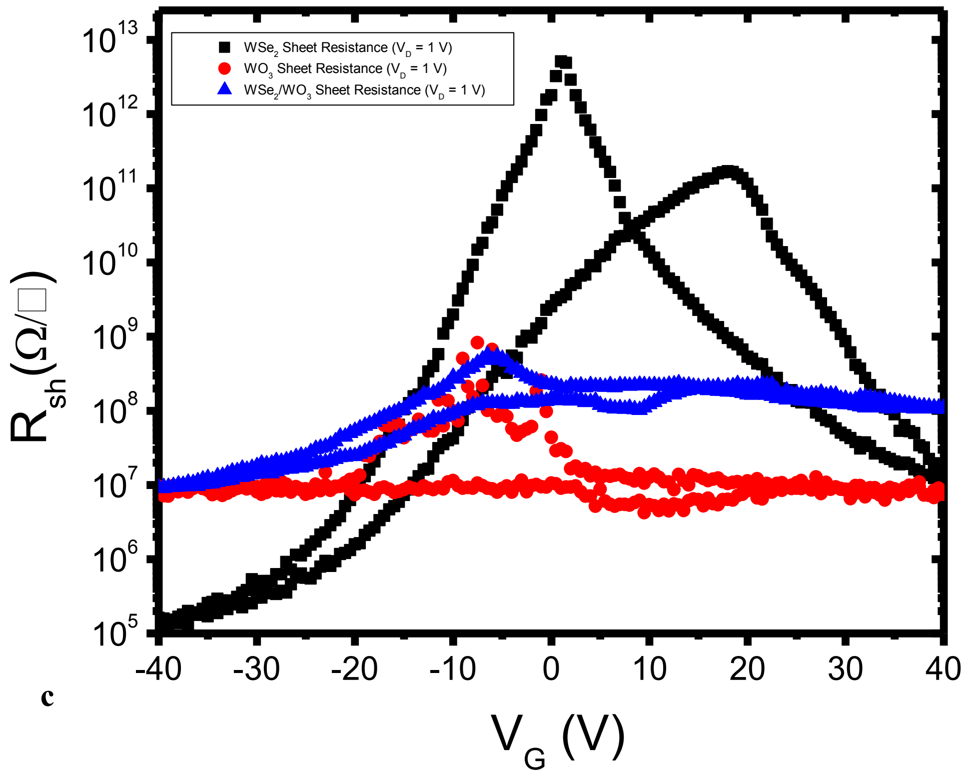

c

Figure 5.5. (a) Optical image of the device fabricated with Pd four point probes on 90 nm SiO_2/Si. (b) Sheet resistances of the WSe_2, WOx, and WSe_2/WOx interface as a function of the drain voltage with no gate bias. WSe_2 is observed to have the highest sheet resistance. (c) Sheet resistance as a function of the gate voltage. WSe_2 sheet resistance experiences significant gate modulation, approaching that of WOx at 40 V and drops below that of WOx and – 40 V. The other two however, show little gate control comparatively.

Chapter 6: Summary and Future Work

6.1 Summary

This work focused on the characterization and development of WSe_2-based devices and oxide structures. WSe_2 flakes were exfoliated and characterized via Raman spectroscopy, MIM, AFM, etc. These flakes were then fabricated into field effect transistors with Pd contacts using electron beam lithography. The devices fabricated showed both p-type conduction and ambipolar conduction, which varied from device to device. Hysteresis was observed for devices measured in ambient atmosphere, but was greatly decreased for those measured in vacuum. The devices exhibited high on/off ratios on the I_D-V_G curve as well as current saturation on the I_D-V_D curve. The low field carrier mobility was extracted to be ~50 $cm^2/V\cdot s$ using the Y function method, and the upper limit of the contact resistance was approximated to be ~ 60 $\Omega\cdot$mm.

Exfoliated WSe_2 flakes were also oxidized via thermal oxidation. The oxidation process was characterized to be anisotropic, progressing primarily around the edges and surface defects. TEM revealed the center of the flakes to unaltered and the edges to be polycrystalline. The oxides were shown to have similar Raman signature as monoclinic (V) and triclinic (VI) WO_3. In addition, MIM shows the oxides to have a higher conductivity at the oxidation front, but the conductivity is then lowered with further oxidation.

This thesis shows that WSe_2 could also be oxidized by a 488 nm Raman laser. The Raman signature is similar to that of the thermally oxidized WSe_2, but the WSe_2 Raman signature is observed to remain, likely due to the underlying unoxidized WSe_2, as shown from ToFSIMS. Using this method, WSe_2 flakes could be selectively oxidized and patterned. The electrical properties of the materials were measured via MIM and devices. It was observed in both methods that the oxidized region was more conductive than WSe_2 without a back gate voltage applied.

To summarize, the properties of WSe_2 and its derived oxide structures have been studied. Such structures hold future possibilities for integration with WSe_2 based applications.

6.2 Future work

Future work would focus on the integration of WO_3 into WSe_2 based applications, such as contact material for devices. Having a WSe_2 derived oxide could also mean WSe_2-based material systems similar to that of the Si/SiO_2 system. This also introduces the possibilities of other TMDC materials and their potential for such material systems. Exploration of other materials and their structures would be a worthwhile direction to pursue. More research could also uncover better processing conditions for the production of these oxides, leading to better quality structures and devices. An additional option to explore is to utilize the electro chromic properties of WO_3.

Bibliography

[1] K. Novoselov, A. Geim, S. Morozov, D. Jiang, M. Katsnelson, I. Grigorieva*, et al.*, "Two-dimensional gas of massless Dirac fermions in graphene," *Nature,* vol. 438, pp. 197-200, 2005.

[2] Y. Zhang, Y.-W. Tan, H. Stormer, and P. Kim, "Experimental observation of the quantum Hall effect and Berry's phase in graphene," *Nature,* vol. 438, pp. 201-204, 2005.

[3] N. Petrone, I. Meric, J. Hone, and K. Shepard, "Graphene field-effect transistors with gigahertz-frequency power gain on flexible substrates," *Nano letters,* vol. 13, pp. 121-125, 2013.

[4] J. Lee, T.-J. Ha, H. Li, K. Parrish, M. Holt, A. Dodabalapur*, et al.*, "25 GHz embedded-gate graphene transistors with high-k dielectrics on extremely flexible plastic sheets," *ACS nano,* vol. 7, pp. 7744-7750, 2013.

[5] Y. Zhu, S. Murali, M. D. Stoller, K. J. Ganesh, W. Cai, P. J. Ferreira*, et al.*, "Carbon-based supercapacitors produced by activation of graphene," *Science,* vol. 332, pp. 1537-41, Jun 24 2011.

[6] A. N. Grigorenko, M. Polini, and K. S. Novoselov, "Graphene plasmonics," *Nat Photon,* vol. 6, pp. 749-758, 11//print 2012.

[7] Y.-M. Lin, C. Dimitrakopoulos, K. A. Jenkins, D. B. Farmer, H.-Y. Chiu, A. Grill*, et al.*, "100-GHz Transistors from Wafer-Scale Epitaxial Graphene," *Science,* vol. 327, p. 662, February 5, 2010 2010.

[8] L. Yu, "Two-dimensional Materials for Ubiquitous Electronics," Master of Science, Electrical Engineering and Computer Science, Massachusetts Institute of Technology, 2013.

[9] C. R. Dean, A. F. Young, I. Meric, C. Lee, L. Wang, S. Sorgenfrei*, et al.*, "Boron nitride substrates for high-quality graphene electronics," *Nat Nanotechnol,* vol. 5, pp. 722-6, Oct 2010.

[10] J. Xue, J. Sanchez-Yamagishi, D. Bulmash, and P. Jacquod…, "Scanning tunnelling microscopy and spectroscopy of ultra-flat graphene on hexagonal boron nitride," *Nature materials,* 2011.

[11] L. Wang, Z. Chen, C. Dean, T. Taniguchi, K. Watanabe, L. Brus*, et al.*, "Negligible environmental sensitivity of graphene in a hexagonal boron nitride/graphene/h-BN sandwich structure," *ACS nano,* vol. 6, pp. 9314-9319, 2012.

[12] Q. H. Wang, K. Kalantar-Zadeh, A. Kis, J. N. Coleman, and M. S. Strano, "Electronics and optoelectronics of two-dimensional transition metal dichalcogenides," *Nat Nanotechnol,* vol. 7, pp. 699-712, Nov 2012.

[13] A. Geim and I. Grigorieva, "Van der Waals heterostructures," *Nature,* vol. 499, pp. 419-425, 2013.

[14] S. Haigh, A. Gholinia, R. Jalil, S. Romani, L. Britnell, D. Elias*, et al.*, "Cross-sectional imaging of individual layers and buried interfaces of graphene-based heterostructures and superlattices," *Nature materials,* vol. 11, pp. 764-767, 2012.
[15] A. Kuc, N. Zibouche, and T. Heine, "Influence of quantum confinement on the electronic structure of the transition metal sulfide TS_{2}," *Physical Review B,* vol. 83, 2011.
[16] B. Radisavljevic, A. Radenovic, J. Brivio, V. Giacometti, and A. Kis, "Single-layer MoS2 transistors," *Nat Nanotechnol,* vol. 6, pp. 147-50, Mar 2011.
[17] W. Liu, J. Kang, D. Sarkar, Y. Khatami, D. Jena, and K. Banerjee, "Role of metal contacts in designing high-performance monolayer n-type WSe2 field effect transistors," *Nano Lett,* vol. 13, pp. 1983-90, May 8 2013.
[18] H. Wang, L. Yu, Y.-H. Lee, Y. Shi, A. Hsu, M. Chin*, et al.*, "Integrated circuits based on bilayer MoS_2 transistors," *Nano letters,* vol. 12, pp. 4674-4680, 2012.
[19] H.-Y. Chang, S. Yang, J. Lee, L. Tao, W.-S. Hwang, D. Jena*, et al.*, "High-performance, highly bendable MoS2 transistors with high-k dielectrics for flexible low-power systems," *ACS nano,* vol. 7, pp. 5446-5452, 2013.
[20] O. Lopez-Sanchez, D. Lembke, M. Kayci, A. Radenovic, and A. Kis, "Ultrasensitive photodetectors based on monolayer MoS2," *Nature nanotechnology,* vol. 8, pp. 497-501, 2013.
[21] T. Georgiou, R. Jalil, B. Belle, L. Britnell, R. Gorbachev, S. Morozov*, et al.*, "Vertical field-effect transistor based on graphene-WS2 heterostructures for flexible and transparent electronics," *Nature nanotechnology,* vol. 8, pp. 100-103, 2013.
[22] S. Chuang, C. Battaglia, A. Azcatl, S. McDonnell, J. Kang, X. Yin*, et al.*, "MoS2 P-type Transistors and Diodes Enabled by High Work Function MoOx Contacts," *Nano letters,* vol. 14, pp. 1337-1342, 2014.
[23] M. Benameur, B. Radisavljevic, J. Héron, S. Sahoo, H. Berger, and A. Kis, "Visibility of dichalcogenide nanolayers," *Nanotechnology,* vol. 22, p. 125706, 2011.
[24] A. Kumar and P. K. Ahluwalia, "Electronic structure of transition metal dichalcogenides monolayers 1H-MX2 (M = Mo, W; X = S, Se, Te) from ab-initio theory: new direct band gap semiconductors," *The European Physical Journal B,* vol. 85, 2012.
[25] H. Zeng, G.-B. Liu, J. Dai, Y. Yan, B. Zhu, R. He*, et al.*, "Optical signature of symmetry variations and spin-valley coupling in atomically thin tungsten dichalcogenides," *Scientific reports,* vol. 3, p. 1608, 2013.
[26] H. Terrones, E. D. Corro, S. Feng, J. M. Poumirol, D. Rhodes, D. Smirnov*, et al.*, "New First Order Raman-active Modes in Few Layered Transition Metal Dichalcogenides," *Scientific Reports,* vol. 4, 2014.
[27] H. Li, G. Lu, Y. Wang, Z. Yin, C. Cong, Q. He*, et al.*, "Mechanical exfoliation and characterization of single- and few-layer nanosheets of WSe_2 , TaS_2 , and $TaSe_2$," *Small (Weinheim an der Bergstrasse, Germany),* vol. 9, pp. 1974-1981, 2013.

[28] G. Ghibaudo, "New method for the extraction of MOSFET parameters," *Electronics Letters,* 1988.
[29] H. Chang, W. Zhu, and D. Akinwande, "On the mobility and contact resistance evaluation for transistors based on MoS2 or two-dimensional semiconducting atomic crystals," *Applied Physics Letters,* 2014.
[30] V. Podzorov, M. E. Gershenson, K. Ch, R. Zeis, and E. Bucher, "High-mobility field-effect transistors based on transition metal dichalcogenides," *Applied Physics Letters,* vol. 84, 2004.
[31] S. McDonnell, R. Addou, C. Buie, R. Wallace, and C. Hinkle, "Defect-Dominated Doping and Contact Resistance in MoS2," *ACS nano,* 2014.
[32] A. G. Souza-Filho, V. N. Freire, J. M. Sasaki, J. M. Filho, J. F. Juli�o, and U. U. Gomes, "Coexistence of triclinic and monoclinic phases in WO3 ceramics," *Journal of Raman Spectroscopy,* vol. 31, 2000.
[33] E. Salje, "Lattice dynamics of WO3," *Acta Crystallographica Section A: Crystal Physics, Diffraction, Theoretical and General Crystallography,* vol. 31, pp. 360-363, 1975.
[34] S. M. Felicia, L. E. Jose, G. D. William, Y. Young, V. R. Chintalapalle, and K. G. Satya, "Spectroscopic analysis of tungsten oxide thin films," *Journal of Materials Research,* vol. 25, 2011.